GeoScienceWorld
Lithosphere
Volume 2022, Article ID 8377620, 19 pages
https://doi.org/10.2113/2022/8377620

Lithosphere

Research Article

Petrogenesis of Paleozoic–Early Mesozoic Granites and Pegmatites in the Yuechengling Pluton of South China

Xiao Liu,[1,2] Xi-Jun Liu,[1,2,3] Wei Fu,[1] Yu Shi,[1,2] Jing-Lian Guo,[1] Rong-Guo Hu,[1,2] Chuan Zhao,[1] Meng Feng,[1] Zheng-Lin Li,[1] and Xianzhu Qin[1]

[1]*Guangxi Key Laboratory of Hidden Metallic Ore Deposits Exploration, College of Earth Sciences, Guilin University of Technology, Guilin 541004, China*
[2]*Collaborative Innovation Center for Exploration of Nonferrous Metal Deposits and Efficient Utilization of Resource, Guilin University of Technology, Guilin 541004, China*
[3]*Xinjiang Research Center for Mineral Resources, Xinjiang Institute of Ecology and Geography, Chinese Academy of Sciences, Urumqi 830011, China*

Correspondence should be addressed to Xi-Jun Liu; xijunliu@glut.edu.cn

Received 19 May 2022; Accepted 21 July 2022; Published 5 August 2022

Academic Editor: Jiyuan Yin

Although pegmatites are volumetrically minor in the upper continental crust, these rocks host abundant rare metal deposits (e.g., Li, Be, Rb, Ta, and Nb). Pegmatites can be formed either by extensive fractional crystallization of granitic magmas or by low-degree partial melting of metasedimentary rocks. The Mao'ershan–Yuechengling composite batholith in the Nanling Range in the South China Block (SCB) is of early Paleozoic–Triassic age (440–381 and 236–204 Ma, respectively). Recently, hundreds of pegmatites associated with Nb, Ta, Be, Rb, and Li mineralization have been identified in this batholith. These pegmatites are hosted by granitic wall rocks. However, the relationships between the pegmatites and granitic wall rocks are not well constrained. To address this, we investigated the Mao'antang (MAT) and Tongzuo (TZ) pegmatites and their biotite granite wall rocks in the middle part of the Yuechengling pluton. Laser ablation inductively coupled plasma mass spectrometry zircon U–Pb ages revealed that the MAT pegmatites formed during the Permian (269 Ma) and Triassic (231 Ma) and that the MAT biotite granite wall rock records two stages of magmatic activity (271 and 231 Ma) that are coeval with the pegmatites. The TZ pegmatites probably formed during the Triassic (235 Ma), and the TZ biotite granite wall rock formed during the Silurian (435 Ma). The MAT biotite granite and pegmatites ($\varepsilon_{Nd}(t) = -12.0$ to -10.6; $\varepsilon_{Hf}(t) = -8.0$ to -1.0), TZ pegmatites ($\varepsilon_{Nd}(t) = -10.4$ to -6.1), and TZ biotite granites ($\varepsilon_{Nd}(t) = -9.1$ to -8.7; $\varepsilon_{Hf}(t) = -7.7$ to -4.1) have enriched whole-rock Nd and zircon Hf isotopic compositions that are similar to those of early Paleozoic and Triassic S-type granites in the SCB. In addition, the whole-rock Pb isotopic compositions of the MAT and TZ pegmatites and granites are distributed along the upper crust evolution line. We suggest that the MAT and TZ biotite granites were mainly derived from Paleoproterozoic metasedimentary rocks in the middle crust. The MAT pegmatites are fractional crystallization products of the MAT biotite granites, whereas the TZ pegmatites were formed by fractional crystallization of hidden parental S-type granites. We propose that the MAT and TZ pegmatites have potential for rare metal (Nb, Ta, Be, and Li) mineralization, as they record high degrees of fractional crystallization. The MAT and TZ areas in the middle of the Yuechengling pluton are promising targets for rare metal exploration.

1. Introduction

Strategic resources and critical materials are of significance to science, technology, and the economy and have the greatest risk of supply disruptions. These materials include Li, Be, Ta, Nb, and rare earth elements [1, 2]. Pegmatites are an important source of rare metal elements (Li, Be, Ta, and Nb), and they are texturally complex igneous rocks marked by some combination of coarse and variable crystal sizes, mineralogical zonation, prominent anisotropy of crystal

orientations from their margins inward, and crystals with skeletal, radial, and graphic-intergrowth habits [3]. Pegmatites commonly have a granitic composition with high contents of fluxing components such as H_2O, F, B, P, and alkalis, and they are therefore generally considered to represent the final products of extreme differentiation of an evolving granite system (e.g., [3]). However, in the field, there are occasions when no granite plutons occur near pegmatites, as observed for the Qinghe pegmatites in the Altai Orogen (NW China; [4]). An alternative model suggests that pegmatites may be formed as result of thrusting-enhanced low degrees of melting of metapelitic rocks at relatively low temperatures (amphibolite-facies conditions in the middle crust) during compressional deformation in an orogenic belt [4–6]. Studies of the petrogenesis of rare metal pegmatites and granitic wall rocks have economic significance, as the results serve as a guide during prospecting for rare metal ore deposits [7].

The Nanling Range covers six provinces (Guizhou, Guangxi, Hunan, Guangdong, Jiangxi, and Fujian) in the southern part of South China, and it is endowed with various W, Sn, Bi, and Sb deposits [8]. Recent geological surveys in the western Nanling Range have identified several hundred pegmatites in the Mao'ershan–Yuechengling composite batholith. These pegmatites are associated with Nb, Ta, Be, Li, and Rb mineralization [9]. However, the ages of these pegmatites have not been well constrained, and the genetic relationships between the pegmatites and their granitic wall rocks remain unclear. In this paper, we present the results of a detailed petrographic, geochronological, and geochemical study (including whole-rock Sr–Nd–Pb and zircon Hf isotopic data) of the Mao'antang (MAT) and Tongzuo (TZ) pegmatites and their biotite granite wall rocks in the middle part of the Yuechengling pluton. Our results enable us to constrain the petrogenesis of the pegmatites and biotite granites and to provide important insights into the relationships between magma generation and rare metal mineralization in the Nanling Range.

2. Geological Setting and Sample Descriptions

The South China Block (SCB) comprises the Yangtze Block to the northwest and the Cathaysia Block to the southeast (Figure 1(a)), which were amalgamated during a Neoproterozoic continent–continent collisional orogeny (i.e., the Jiangnan Orogen; [10] and references therein). The basement of the Cathaysia Block consists of Paleoproterozoic–Mesoproterozoic–Neoproterozoic metasedimentary rocks that include two-mica schists, mica–quartz schists, and biotite–plagioclase granulites and metaigneous rocks (amphibolites; [11–13]). The basement of the eastern Yangtze Block is the Mesoproterozoic Lengjiaxi Group, which consists of greenschist- to amphibolite-facies meta-tholeiitic basalts and basaltic andesites with subordinate pelites [14]. The metamorphic basement of the SCB was overlain by late Neoproterozoic to early Paleozoic Nanhua rift sediments [15]. An early Paleozoic intracontinental orogeny closed the Nanhua rift, resulting in deformation and metamorphism of the pre-Devonian rocks [16]. In response to the early Paleozoic intracontinental orogeny, large amounts of granites and minor mafic rocks were formed in the Wuyi, Yunkai, Wugong, and Baiyun domains ([10, 16, 17]; Figure 1(b)). During the Middle or Late Devonian to Permian, the SCB evolved into a stable littoral–neritic depositional environment where Brachiopoda-, coral-, and fusulina-bearing carbonates (limestones and dolomites), black cherts, and minor sandstones and mudstones accumulated ([15] and references therein). During the Middle–Late Triassic, a series of thrust and strike-slip faults, ductile shear zones, and widespread granites developed in the SCB ([18] and references therein). Some previous studies have suggested that the Triassic orogeny resulted from the collision between the Indochina Block and SCB [18–21]. Other studies have proposed that the Triassic orogeny and associated magmatism were related to flat slab subduction of the Paleo-Pacific Plate [22]. Moreover, Mao et al. [23] suggested that the Triassic orogeny and associated magmatism might have been caused by the collision between the Southeast Asian continental margin and Paleo-Pacific Plate. The tectonic setting of the SCB changed gradually from one of compression to one of extension during the late Mesozoic [21]. In the Jurassic and Cretaceous, the SCB was characterized by magmatic flare-ups, and 80% of the SCB igneous rocks (which have a total exposed area of >200,000 km^2) were formed during this period [21, 24].

The Mao'ershan–Yuechengling granitic batholith lies near the Anhua–Luocheng Fault (Figure 1(b)). It extends northeast from north Guangxi Province to southern Hunan Province and has an outcrop area of ~3400 km^2 (Figures 1(b) and 2). Most of the Mao'ershan–Yuechengling granites were formed during the early Paleozoic at 440–381 Ma [28–30]. These early Paleozoic granitic rocks were emplaced into the core of the Mao'ershan–Yuechengling anticlinorium, which is made up of Neoproterozoic–Silurian slates, pelitic schists, felsic volcaniclastics, metasandstones, and marbles. In some outcrops, the Mao'ershan–Yuechengling granites are overlain by Middle Devonian sedimentary rocks ([30] and references therein). The early Paleozoic Mao'ershan–Yuechengling granites were intruded by younger Triassic granites with ages of 236–204 Ma ([31, 32] and references therein). The Mao'ershan–Yuechengling batholith is divided into the Mao'ershan and Yuechengling plutons by the Xinzi Fault. On the surface, the outcrops of these two plutons are separated by Devonian–Cretaceous sedimentary rocks, but at depth, they are connected ([29] and references therein).

The Mao'antang (MAT) and Tongzuo (TZ) pegmatites and their granitic wall rocks are located in the northeastern part of Ziyuan County in the middle of the Yuechengling pluton (Figure 2). The MAT pegmatites are gray in color and typically have massive structures and inequigranular textures. They consist of quartz (40–45 vol.%), K-feldspar (5–10 vol.%), albite (35–40 vol.%), tourmaline (<3 vol.%), and zinnwaldite (<3 vol.%) with minor garnet, muscovite, biotite, allanite, and monazite (Figures 3(a)–3(d)). The MAT pegmatites are mainly muscovite pegmatites, with subordinate biotite and two-mica pegmatites, which generally occur in fractures and cavities in the biotite granite wall rocks (Figure 3(a); Supplementary Figures 1a–1b). In addition, the

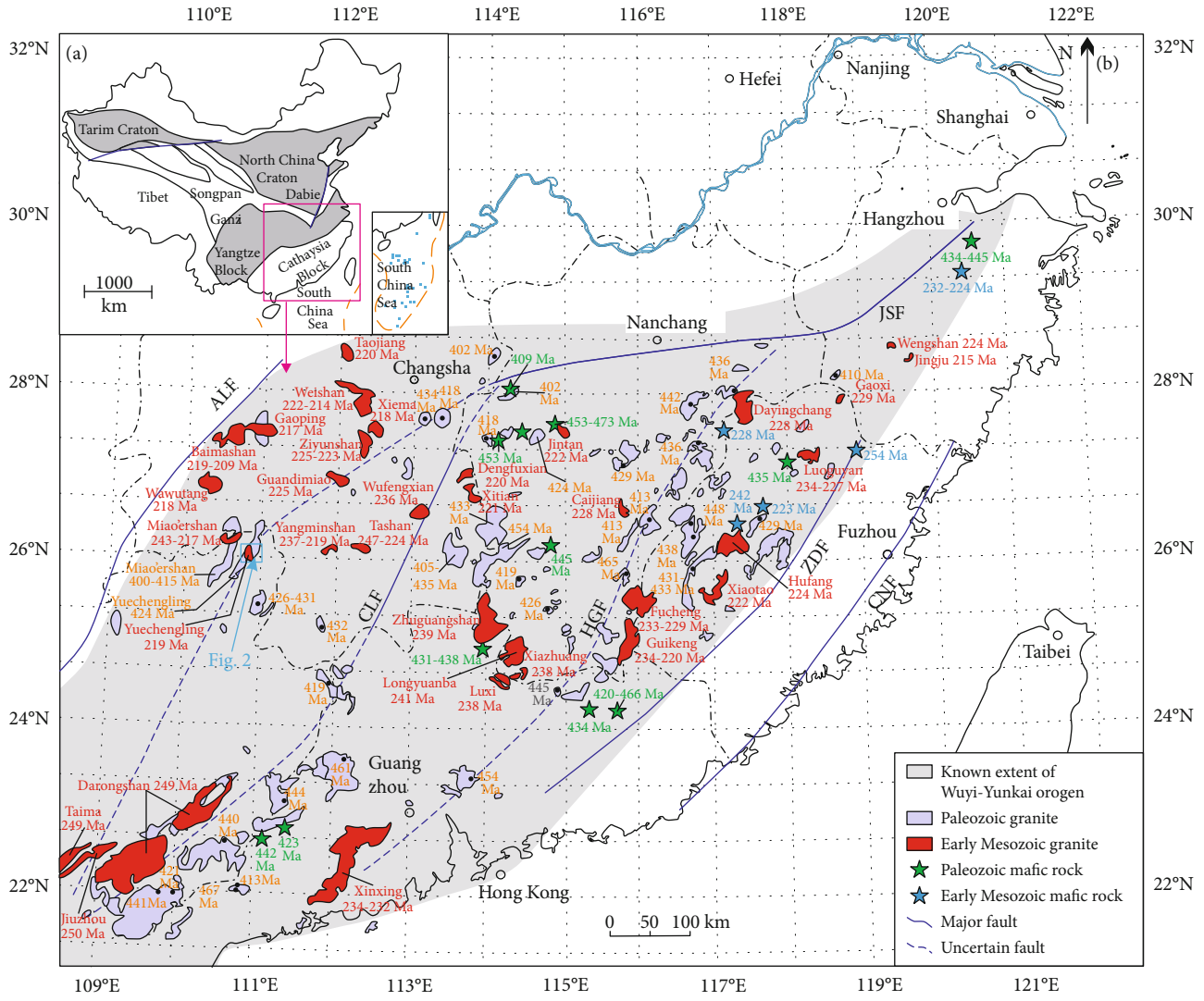

FIGURE 1: (a) Simplified regional map showing the tectonic framework of China (revised from [25]). (b) Sketch map showing the distribution of Paleozoic and Mesozoic magmatic rocks in the South China Block (SCB). Age data for Paleozoic and Mesozoic magmatic rocks are from Liu et al. [26] and Qing et al. [18]. CNF: Changle–Nanao Fault; ZDF: Zhenghe–Dabu Fault; HGF: Heyuan–Guangfeng Fault; CLF: Chenzhou–Linwu Fault; JSF: Jiangshan–Shaoxing Fault; ALF: Anhua–Luocheng Fault. The solid blue line is the Yangtze River, and dotted black lines are provincial borders.

MAT pegmatites are related to Nb, Ta, Be, and Li mineralization. They contain Nb–Ta–Be–Li oxide minerals, such as columbite-group minerals, microlite, wodginite, beryl, and spodumene ([9] and references therein). From the outer to inner zones of the MAT pegmatites, the microcline and muscovite contents decrease, whereas the albite contents increase. As such, the Nb, Ta, and Be contents are gradually enriched from the northwest (outer zone) to southeast (inner zone) ([9] and references therein). The wall rocks of the MAT pegmatites are massive biotite granites that consist of quartz, K-feldspar, albite, biotite, and minor muscovite (Figure 3(a); Supplementary Figures 1a–1b).

The TZ pegmatites are gray in color and typically have massive structures and inequigranular–porphyritic textures. They consist of quartz (30–35 vol.%), K-feldspar (25–30 vol.%), albite (15–20 vol.%), garnet (5–10 vol.%), and muscovite (5 vol.%) with minor monazite and chlorite (Figures 3(f)–3(h)). From the outer to inner zones, the TZ pegmatites change gradually from coarse-grained albite pegmatite to medium-grained graphic albite pegmatite, medium–fine-grained albite pegmatite, and quartz pegmatite (Figure 3(f); Supplementary Figures 1c–1d). The TZ pegmatites are also related to Nb, Ta, and Be mineralization and contain columbite-group minerals, microlite, wodginite, and beryl ([9] and references therein). The wall rocks of the Tongzuo pegmatites are gneissic biotite granites composed of quartz, plagioclase, biotite, and minor muscovite (Figure 3(e); Supplementary Figures 1e–1f).

3. Analytical Methods

Zircon U–Pb dating and Lu–Hf isotope analyses, whole-rock major and trace element geochemical analyses, and Sr–Nd–Pb isotope analyses were carried out at the Guangxi Key

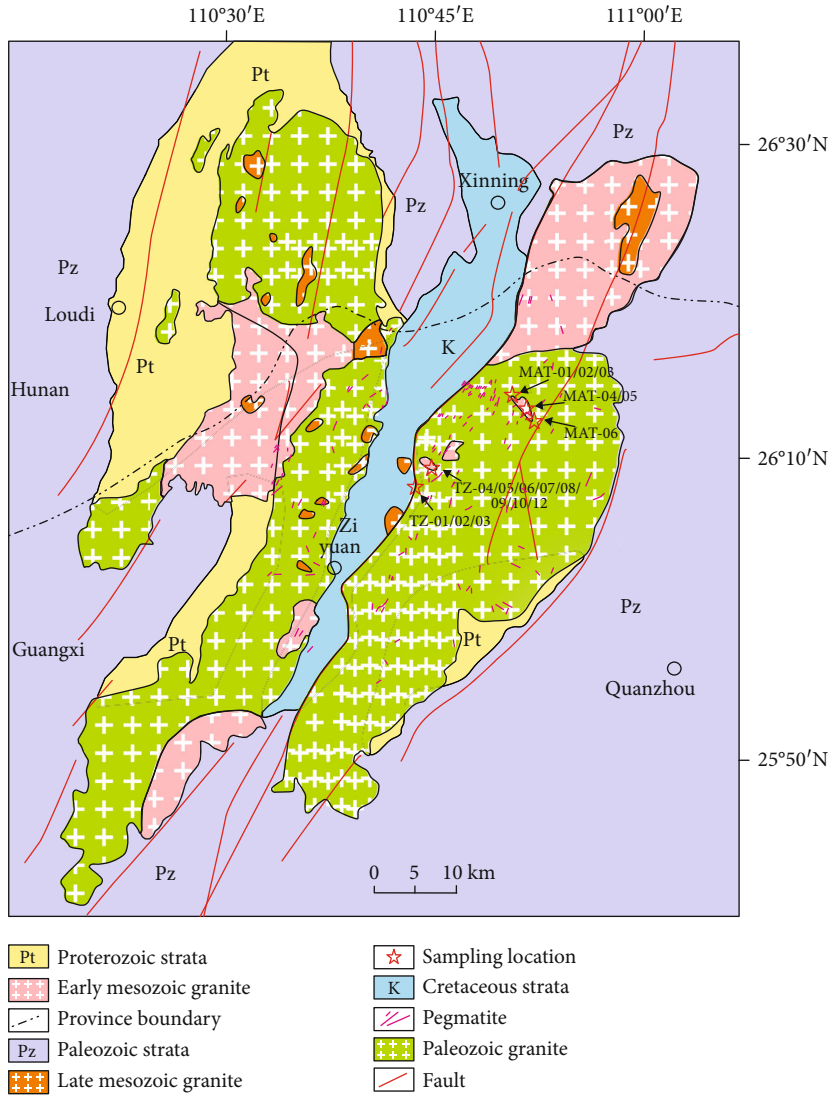

FIGURE 2: Simplified geological map of the Mao'ershan and Yuechengling plutons, modified after Chen et al. [27].

Laboratory of Hidden Metallic Ore Deposits Exploration, Guilin University of Technology, China.

3.1. Zircon U–Pb Geochronology. Zircon grains were separated from ~2 kg rock samples using conventional heavy liquid and magnetic separation techniques. Zircon grains were handpicked and mounted on an epoxy resin disc and polished prior to analysis with a laser ablation inductively coupled plasma mass spectrometer (LA–ICP–MS). Cathodoluminescence (CL) imaging of the zircon grains was performed at the Chongqing Yujin Technology Co., Ltd., China. The U–Pb isotopic compositions of zircon grains from the MAT and TZ pegmatites and granite wall rocks were analyzed using an Agilent 7500 LA–ICP–MS. Laser ablation was undertaken at a constant energy of 80 mJ, a repetition rate of 6 Hz, and a spot size of 32 μm. Helium was used to carry ablated material to the ICP–MS. Element corrections were determined relative to the standard glass NIST 610 [33]. During our analytical work, the zircon standard Plešovice yielded a weighted-mean $^{206}Pb/^{238}U$ age of 337.1 ± 0.6 Ma (2σ; MSWD = 0.10; $n = 52$), which is within error of the recommended value of 337.1 ± 0.4 Ma [34]. The age calculations were undertaken using ICPMSDataCal (version 8.4; [35]), and the concordia plots were made using Isoplot 3.75 [36].

3.2. Major and Trace Element Analyses. Rock samples were first examined under an optical microscope. Selected whole-rock samples were broken into small chips and cleaned ultrasonically in 4 N hydrochloric acid for 30 min to remove any altered material and then washed twice with distilled water. The small rock chips were dried and handpicked to remove visible contamination. The powder was used for analyses of major and trace elements as well as Sr–Nd–Pb isotopes. Major elements were analyzed on fused glass beads using a ZSX Primus II X-ray fluorescence (XRF) spectrometer with analytical uncertainties < 5% ([37] and references therein). Trace elements were analyzed with Agilent 7500cx ICP–MS equipment, following the procedures described by Liu et al. [37]. Analytical precisions for most

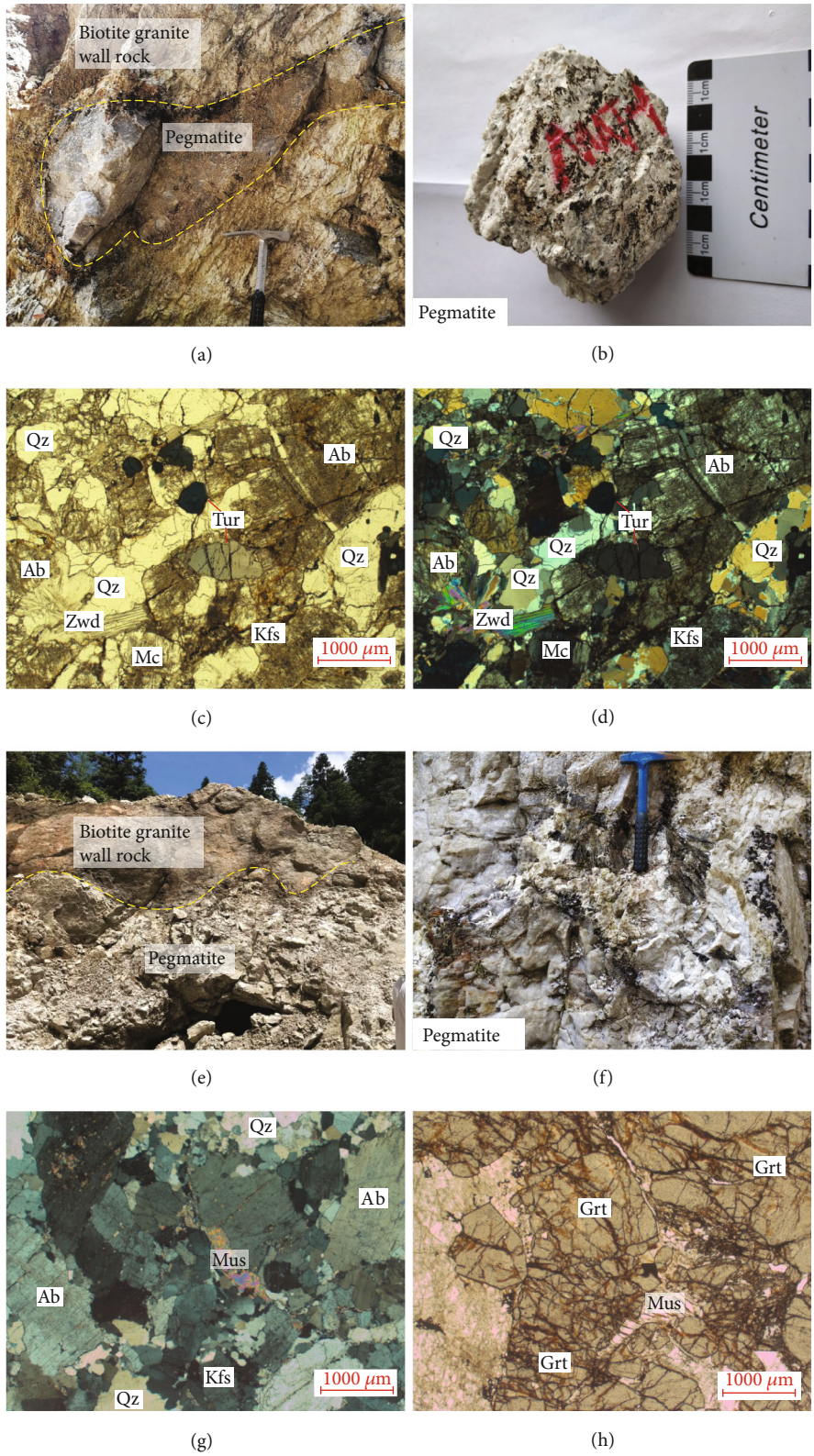

FIGURE 3: Outcrop and hand sample photographs and photomicrographs of the Mao'antang (MAT) and Tongzuo (TZ) biotite granites and pegmatites. (a–b) MAT granite and pegmatites. (c–d) MAT pegmatite. (e–f) TZ granite and pegmatites. (g–h) TZ pegmatites. Photomicrographs (c) and (h) were taken under plane-polarized light, while (d) and (g) were taken under crosspolarized light. Qz: quartz; Ab: albite; Mc: microcline; Zwd: zinnwaldite; Kfs: K-feldspar; Tur: tourmaline; Mus: muscovite; Grt: garnet.

elements were better than ±2–5% (relative standard deviation, RSD). Standardization was achieved using the United States Geological Survey (USGS) standards BHVO, AGV, W-2, and G-2 and national rock standards GSR-1, GSR-2, and GSR-3 [38].

3.3. Sr–Nd–Pb Isotope Analyses. Whole-rock Sr, Nd, and Pb isotope analyses were conducted using a Neptune plus multicollector- (MC-) ICP–MS. The details of the analytical procedures used have been described by Liu et al. [37]. The measured average $^{87}Sr/^{86}Sr$ ratio of the NBS987 standard was 0.710281 ± 16 (2σ; n = 11), and the measured average $^{143}Nd/^{144}Nd$ ratio of the Shin Etsu JNdi-1 standard was 0.512092 ± 8 (2σ; n = 2), which are in good agreement with the recommended values of 0.710248 ± 12 and 0.512107 ± 12, respectively [39]. All measured $^{87}Sr/^{86}Sr$ and $^{143}Nd/^{144}Nd$ ratios were fractionation-corrected to $^{86}Sr/^{88}Sr = 0.1194$ and $^{146}Nd/^{144}Nd = 0.7219$, respectively. Four repeat analyses of the SRM981 Pb standard yielded mean values of $^{206}Pb/^{204}Pb = 16.933 \pm 0.0008$, $^{207}Pb/^{204}Pb = 15.485 \pm 0.0008$, and $^{208}Pb/^{204}Pb = 36.676 \pm 0.0019$, which agree with the values reported by Todt et al. [40].

3.4. In Situ Zircon Lu–Hf Isotope Analyses. In situ zircon Lu–Hf isotope measurements were undertaken using a Neptune MC-ICP–MS with a beam size of 44 μm and a laser frequency of 10 Hz. Details of the instrumental conditions and data acquisition procedures have been described by Wu et al. [41]. The isobaric interference of ^{176}Lu on ^{176}Hf was negligible, due to the extremely low value of $^{176}Lu/^{177}Hf$ in the zircon (normally <0.002). During our analyses, the GJ-1 reference zircon was analyzed as an unknown sample, and it yielded a weighted-mean value of $^{176}Hf/^{177}Hf = 0.281989 \pm 0.000034$ (2σ; n = 22), which is in good agreement with the recommended value of 0.282000 ± 0.000005 [42].

4. Results

4.1. Zircon U–Pb Ages. The results of the zircon U–Pb isotope analyses are given in Supplementary Table 1. Five rock samples, including one MAT biotite granite wall rock, two MAT pegmatites, one TZ biotite granite wall rock, and one TZ pegmatite, were selected for the zircon U–Pb dating. Zircon crystals in these samples have lengths of 150–350 μm and length/width ratios of 1 : 1–3 : 1 (Figures 4(a)–4(e)). Zircon grains in the MAT biotite granite wall rock and pegmatites and in the TZ biotite granite wall rock all exhibit well-developed oscillatory zoning (Figures 4(a)–4(d)) and high Th/U ratios (0.15–1.88; Supplementary Table 1), which indicate a magmatic origin [43]. However, zircon grains in the TZ pegmatite TZ-09 show dark and unclear CL images (Figure 4(e)), which suggest that sample TZ-09 underwent late-stage alteration by hydrothermal fluids.

Zircons from MAT wall rock sample MAT-01 yielded two weighted-mean $^{206}Pb/^{238}U$ ages of 230.9 ± 1.5 Ma (2σ; MSWD = 0.79; n = 13; Figure 5(a)) and 271.0 ± 2.0 Ma (2σ; MSWD = 0.37; n = 12; Figure 5(a)), which indicate that this wall rock records two magmatic events. The zircons from MAT pegmatite samples MAT-03 and MAT-04 yielded weighted-mean $^{206}Pb/^{238}U$ ages of 269.1 ± 1.2 Ma (2σ; MSWD = 1.12; n = 19; Figure 5(b)) and 230.5 ± 1.5 Ma (2σ; MSWD = 0.23; n = 12; Figure 5(c)), respectively. Zircons from the TZ biotite granite wall rock yielded a weighted-mean $^{206}Pb/^{238}U$ age of 434.7 ± 1.4 Ma (2σ; MSWD = 0.57; n = 45; Figure 5(d)). Five zircon grains from TZ pegmatite sample TZ-09 yielded a weighted-mean $^{206}Pb/^{238}U$ age of 234.7 ± 4.8 Ma (2σ; MSWD = 1.4; n = 5; Figure 5(e)), which probably represents the crystallization age of the TZ pegmatite, while another six zircon grains from the same sample (TZ-09) yielded a weighted-mean $^{206}Pb/^{238}U$ age of 261.0 ± 2.9 Ma (2σ; MSWD = 0.05; n = 6; Figure 5(e)), which we interpret to be an inherited age. To summarize, the MAT pegmatites formed during the Permian (269 Ma) and Triassic (231 Ma), the MAT biotite granite wall rocks record two stages of magmatic activity (271 and 231 Ma) that were coeval with the Permian and Triassic pegmatites, the TZ pegmatite probably formed during the Triassic (235 Ma), and the TZ biotite granite wall rock formed during the Silurian (435 Ma).

4.2. Major and Trace Element Geochemistry

4.2.1. MAT and TZ Pegmatites. Whole-rock major and trace element data for the MAT pegmatites and TZ pegmatites and their granite wall rocks are given in Supplementary Table 2. The MAT pegmatites have high contents of SiO_2 (70.2–73.5 wt.%), K_2O (4.2–5.5 wt.%), and Na_2O (0.5–3.9 wt.%), with $K_2O > Na_2O$, and they plot in the high-K calc-alkalic to shoshonitic fields on the K_2O versus SiO_2 diagram (Figures 6(a), 6(b), and 6(d)). Their A/CNK (molar $Al_2O_3/[CaO + Na_2O + K_2O]$) values range from 1.14 to 2.68 and plot in the peraluminous field (Figure 6(c)). The TZ pegmatites have a wide range of SiO_2 (45.0–98.7 wt.%), K_2O (0.01–11.3 wt.%), and Na_2O (0.04–5.65 wt.%) contents (Figures 6(a), 6(b), and 6(d)), and their A/CNK values range from 0.47 to 4.68, plotting in the metaluminous to peraluminous fields (Figure 6(c)). Three TZ pegmatite samples (TZ-07, TZ-08, and TZ-09) have low SiO_2 contents (<61 wt.%; normalized on an anhydrous basis). We do not plot these three pegmatites in Figure 6, because they are cumulates of K-feldspar (SiO_2~65 wt.%), albite (SiO_2~60 wt.%), and muscovite (SiO_2~46 wt.%) (Figured 3(f)–3(g); [26]).

The MAT pegmatites have a wide range of total rare earth element (ΣREE) contents (1.28–203 ppm), and they are characterized by moderately light REE-enriched ($(La/Yb)_{CN}$ = 2.8 – 36.0) chondrite-normalized patterns with significant negative Eu anomalies ($Eu/Eu* = Eu_{CN}/(Sm_{CN} \times Gd_{CN})^{1/2}$ = 0.11 – 0.30) (Figure 7(a)). In addition, the REE patterns of the MAT pegmatites have a gull-wing shape and show tetrad effects (Figure 7(a)). The TZ pegmatites also have a wide range of ΣREE contents (1.00–382 ppm). Their $(La/Yb)_{CN}$ values range from 0.02 to 10.8 (Figure 7(c)), and they are characterized by moderate to significant negative Eu anomalies (Eu/Eu* = 0.01 – 0.44; Figure 7(c)).

On primitive-mantle-normalized plots, the MAT and TZ pegmatites are enriched in Rb, Th, U, and Pb; are slightly to

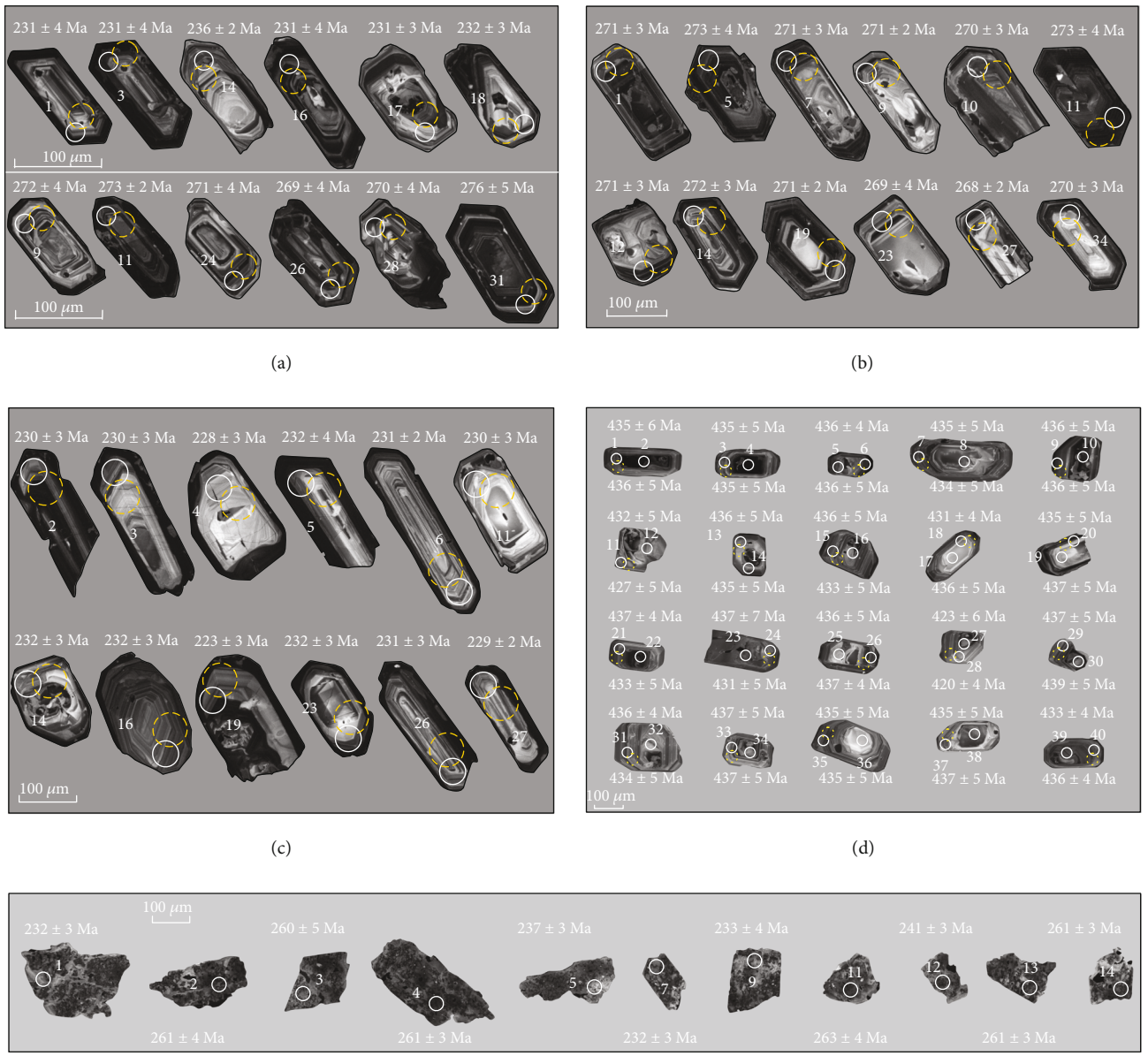

FIGURE 4: Cathodoluminescence (CL) images of zircons from the MAT and TZ biotite granites and pegmatites: (a) MAT-01 (biotite granite); (b) MAT-03 (pegmatite); (c) MAT-04 (pegmatite); (d) TZ-03 (biotite granite); (e) TZ-09 (pegmatite). White solid circles represent LA–ICP–MS zircon age analysis locations; orange dotted circles are MC–LA–ICP–MS zircon Hf isotopic analysis sites.

significantly depleted in Ba, Sr, Zr, and Ti; and show small negative Nb anomalies and slight Ta positive anomalies (Figure 7(b)). The MAT and TZ pegmatites have Nb/Ta ratios of 3.72 to 6.92 and 1.12 to 8.99 and Zr/Hf ratios of 5.34 to 33.8 and 0.80 to 34.5, respectively (Supplementary Table 2).

4.2.2. MAT and TZ Biotite Granite Wall Rocks. The MAT wall rock sample (MAT-01) has a relatively low SiO_2 content of 62.8 wt.% (normalized on an anhydrous basis), which is similar to the diorite (Figure 6(a)). However, sample MAT-01 has obviously lower MgO (0.97 wt.%) and higher Rb (1026 ppm) contents than typical diorites in Guangzhou region of South China (MgO = 2.86 – 2.90 wt.%; Rb = 212 – 217 ppm; [26]). When granitic rocks experience supergene weathering and hydrothermal alteration, their SiO_2 contents decrease as biotite (SiO_2~40 wt.%) is replaced by chlorite (SiO_2~28 wt.%) [51]. This is consistent with the negative Ce anomaly of the MAT biotite granite (Figure 7(a)). Negative Ce anomalies in granites have been interpreted to be related to chemical weathering processes [52]. Therefore, we regard sample MAT-01 to be a biotite granite rather than a diorite. In addition, the MAT biotite granite wall rock has a K_2O content of 5.83 wt.% and plots in the shoshonitic field on the K_2O versus SiO_2 diagram (Figure 6(b)). Moreover, it has A/CNK values of 2.95 and plots in the peraluminous field (Figure 6(c)). The

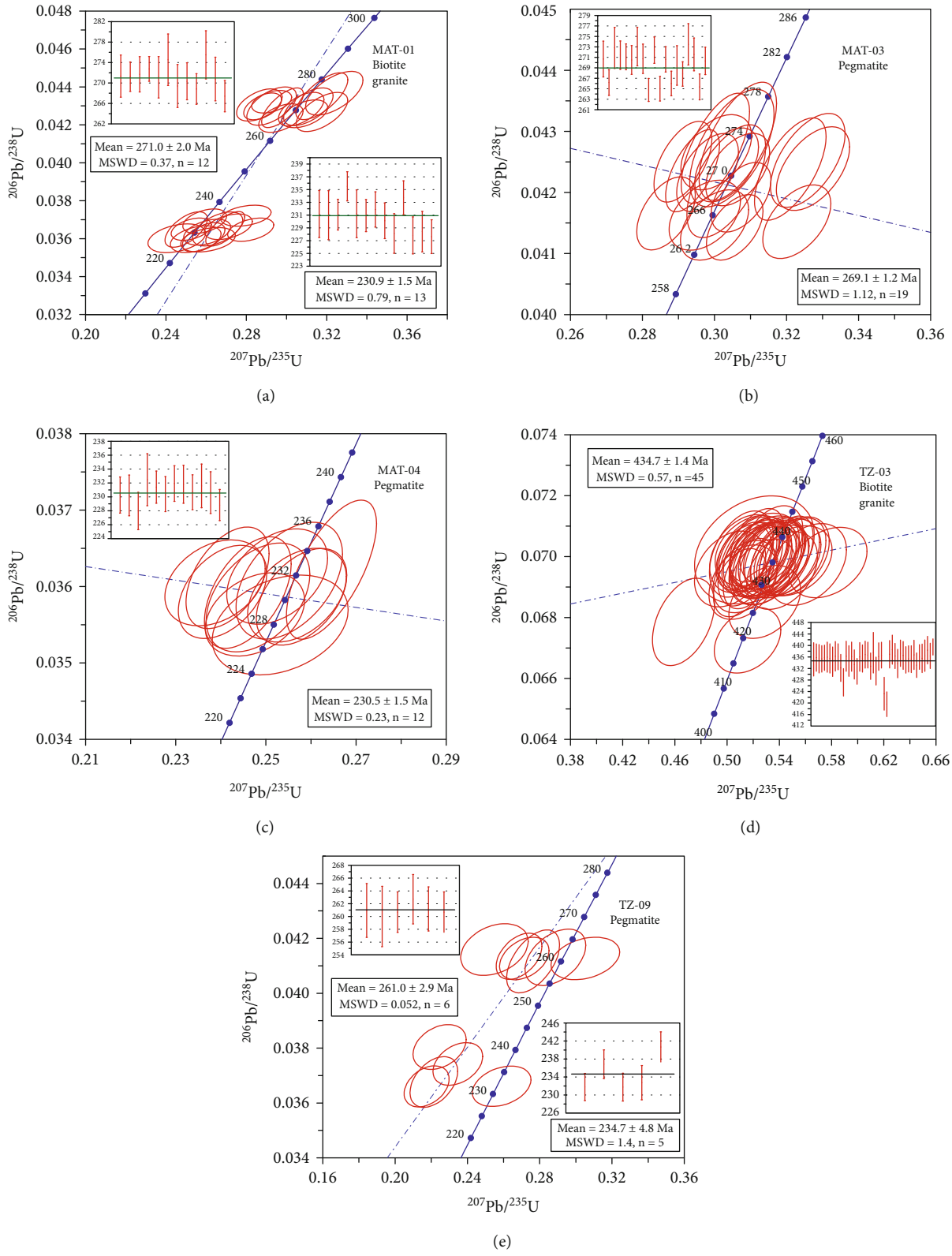

FIGURE 5: LA–ICP–MS zircon U–Pb concordia diagrams: (a) MAT-01 (biotite granite); (b) MAT-03 (pegmatite); (c) MAT-04 (pegmatite); (d) TZ-03 (biotite granite); (e) TZ-09 (pegmatite).

TZ biotite granite wall rocks have SiO_2 contents of 66.1–71.8 wt.%, K_2O contents of 4.47–7.07 wt.%, and Na_2O contents of 4.47–7.07 wt.% (Figures 6(a), 6(b), and 6(d)). They plot in the high-K calc-alkalic to shoshonitic fields on the K_2O versus SiO_2 diagram (Figure 6(b)). Their A/CNK values range from 1.08 to 1.12, plotting in the peraluminous field (Figure 6(c)).

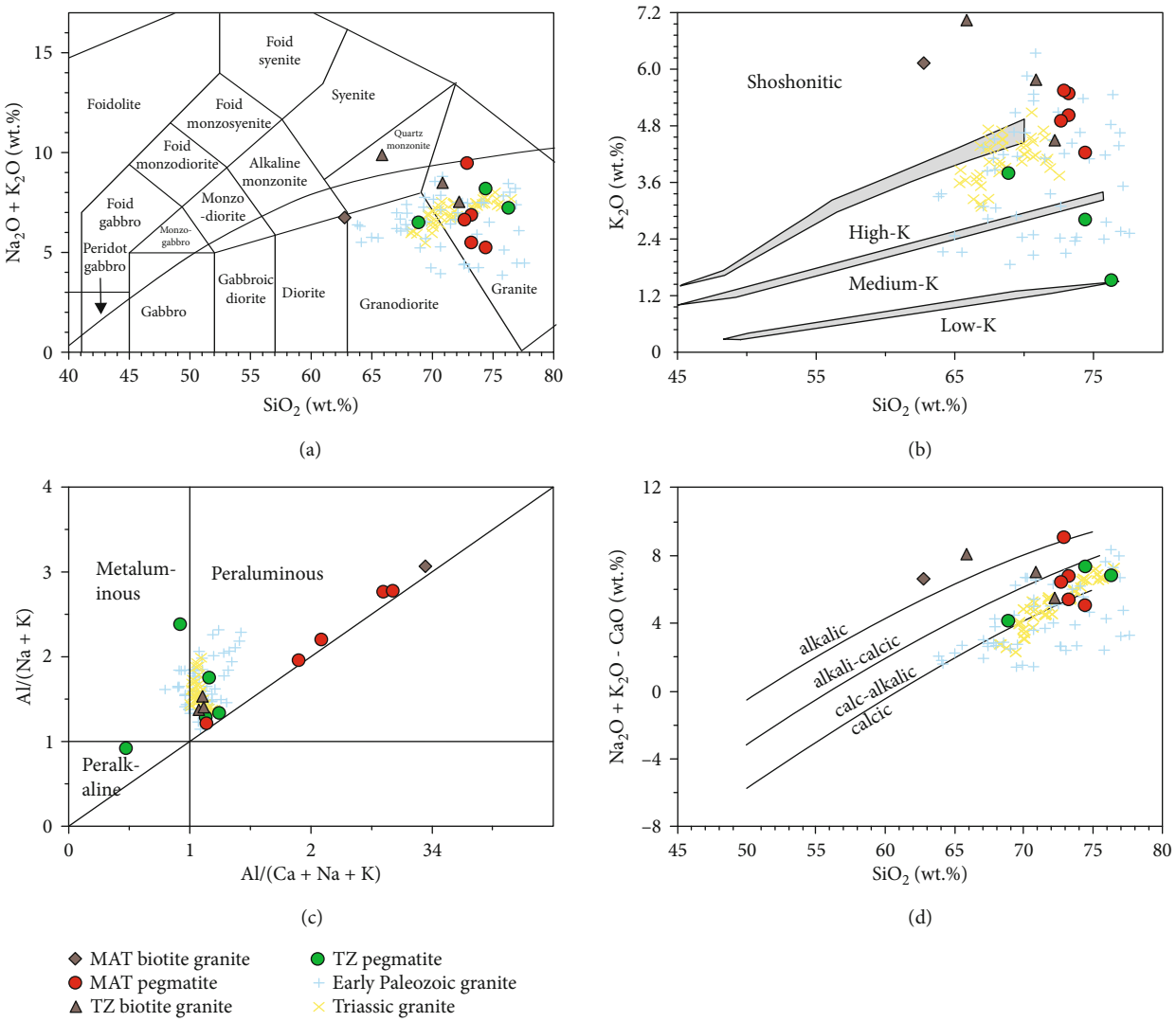

FIGURE 6: Major element classification diagrams for the MAT and TZ biotite granites and pegmatites: (a) total alkalis–silica (TAS) classification diagram (modified from [44]); (b) K_2O versus SiO_2 (modified from [45]); (c) A/NK versus A/CNK (modified from [46]); (d) $Na_2O + K_2O - CaO$ versus SiO_2 (modified from [47]). Data for early Paleozoic granites are from Wang et al. [16] and Zhang et al. [48], and data for Triassic granites are from Wang et al. [20], Gao et al. [49], and Shu et al. [15].

The MAT biotite granite wall rock has a higher ΣREE content (411 ppm) than the MAT pegmatites (Figure 7(a)). The MAT biotite granite wall rock is characterized by slightly light REE-enriched ($(La/Yb)_{CN} = 5.64$) chondrite-normalized patterns with moderate negative Eu anomalies ($Eu/Eu* = 0.21$; Figure 7(a)). The chondrite-normalized REE pattern of the MAT biotite granite wall rock is generally parallel to the REE patterns of the MAT pegmatites (Figure 7(a)). The TZ biotite granite wall rocks have variable ΣREE contents (164.4–498 ppm), and they are characterized by obviously light REE-enriched ($(La/Yb)_{CN} = 14.4 - 29.4$) chondrite-normalized patterns (Figure 7(c)) and moderate to significant negative Eu anomalies ($Eu/Eu* = 0.15 - 0.51$) (Figure 7(c)).

On primitive-mantle-normalized plots, the MAT and TZ biotite granite wall rock is enriched in Rb, Th, U, and Pb and slightly depleted in Ba, Sr, Zr, Hf, and Ti, with small negative Nb anomalies and slight Ta positive anomalies (Figure 7(b)). The trace element pattern of the MAT biotite granite wall rock is generally parallel to the trace element pattern of the MAT pegmatites (Figure 7(b)), and it has Nb/Ta and Zr/Hf ratios of 3.44 and 33.0, respectively (Supplementary Table 2). The TZ biotite granite wall rocks have Nb/Ta ratios that range from 9.54 to 11.6 and Zr/Hf ratios that range from 36.7 to 39.6 (Supplementary Table 2).

4.3. Sr–Nd–Hf–Pb Isotopic Compositions

4.3.1. MAT and TZ Pegmatites. Initial Nd–Pb isotopic ratios were calculated based on the U–Pb ages of zircons in the MAT pegmatites (231 and 269 Ma) and in the TZ pegmatite (235 Ma). Initial Hf isotopic ratios were calculated using the corresponding zircon single-crystal ages. As the MAT and TZ pegmatites have exceptionally high $^{87}Rb/^{86}Sr$ ratios

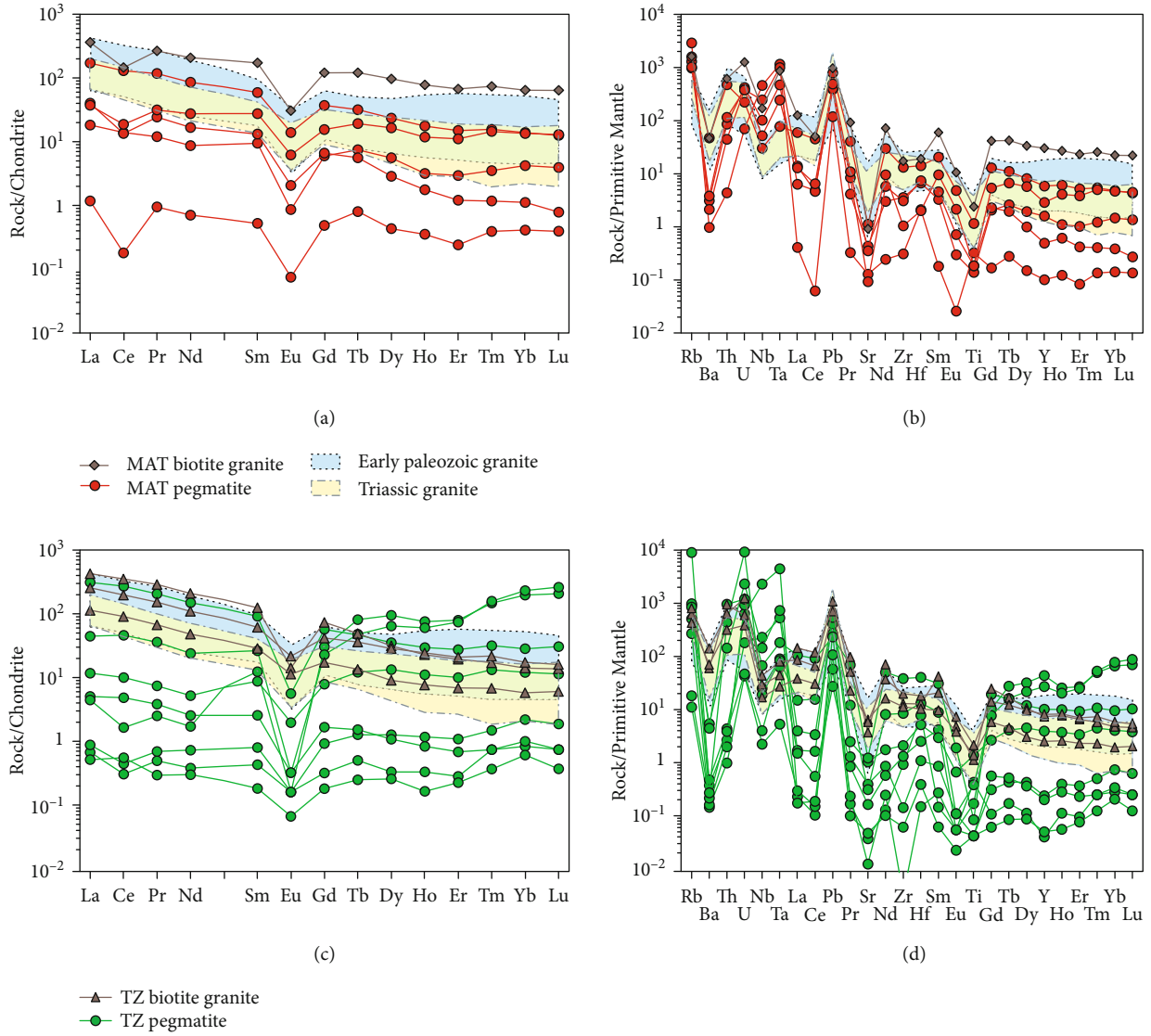

FIGURE 7: (a) Chondrite-normalized REE and (b) primitive-mantle-normalized multielement diagrams for the MAT biotite granites and pegmatites. (c) Chondrite-normalized REE and (d) primitive-mantle-normalized multielement diagrams for the TZ biotite granites and pegmatites. Normalizing values are from Sun and McDonough [50]. Data sources for the early Paleozoic and Triassic granites are the same as for Figure 6.

(57.4 to 260; Supplementary Table 3), we did not calculate their initial $^{87}Sr/^{86}Sr$ ratios. The MAT pegmatites have whole-rock $\varepsilon_{Nd}(t)$ values of −12.0 to −10.7 with two-stage Nd model ages ranging from 2.0 to 1.9 Ga (Supplementary Table 2; Figure 8(a)). The TZ pegmatites have whole-rock $\varepsilon_{Nd}(t)$ values of −10.4 to −6.1, with two-stage Nd model ages ranging from 1.9 to 1.5 Ga (Supplementary Table 2; Figure 8(a)). The ca. 230 Ma MAT pegmatite (MAT-04) yields $\varepsilon_{Hf}(t)$ values of −8.0 to −4.0, with two-stage Hf model ages ranging from 1.8 to 1.5 Ga, whereas the ca. 270 Ma MAT pegmatite (MAT-03) has a wider range of $\varepsilon_{Hf}(t)$ values from −7.8 to −1.0 and two-stage Hf model ages ranging from 1.8 to 1.4 Ga (Supplementary Table 3; Figure 8(b)). The MAT pegmatites have $(^{206}Pb/^{204}Pb)_i$ ratios of 18.555–18.796, $(^{207}Pb/^{204}Pb)_i$ ratios of 15.728–15.736, and $(^{208}Pb/^{204}Pb)_i$ ratios of 38.562–38.789 (Supplementary Table 4; Figure 8(c)). The TZ pegmatite has $(^{206}Pb/^{204}Pb)_i$ ratios of 16.665, $(^{207}Pb/^{204}Pb)_i$ ratios of 15.628, and $(^{208}Pb/^{204}Pb)_i$ ratios of 35.157 (Supplementary Table 4; Figure 8(c)).

4.3.2. MAT and TZ Biotite Granite Wall Rocks. Initial Nd–Pb isotope ratios were calculated based on the zircon U–Pb ages of the MAT biotite granite (271 Ma) and TZ biotite granite (435 Ma). The MAT and TZ biotite granite wall rocks have high $^{87}Rb/^{86}Sr$ ratios (5.6–154; Supplementary Table 2), which preclude the determination of precise whole-rock initial $^{87}Sr/^{86}Sr$ ratios. The MAT biotite granite wall rock has an $\varepsilon_{Nd}(t)$ value of −10.6, with a two-stage Nd model age of 1.9 Ga (Supplementary Table 2; Figure 8(a)). The TZ biotite granite wall rocks have whole-rock $\varepsilon_{Nd}(t)$ values of −9.1 to −8.7, with a consistent two-stage Nd

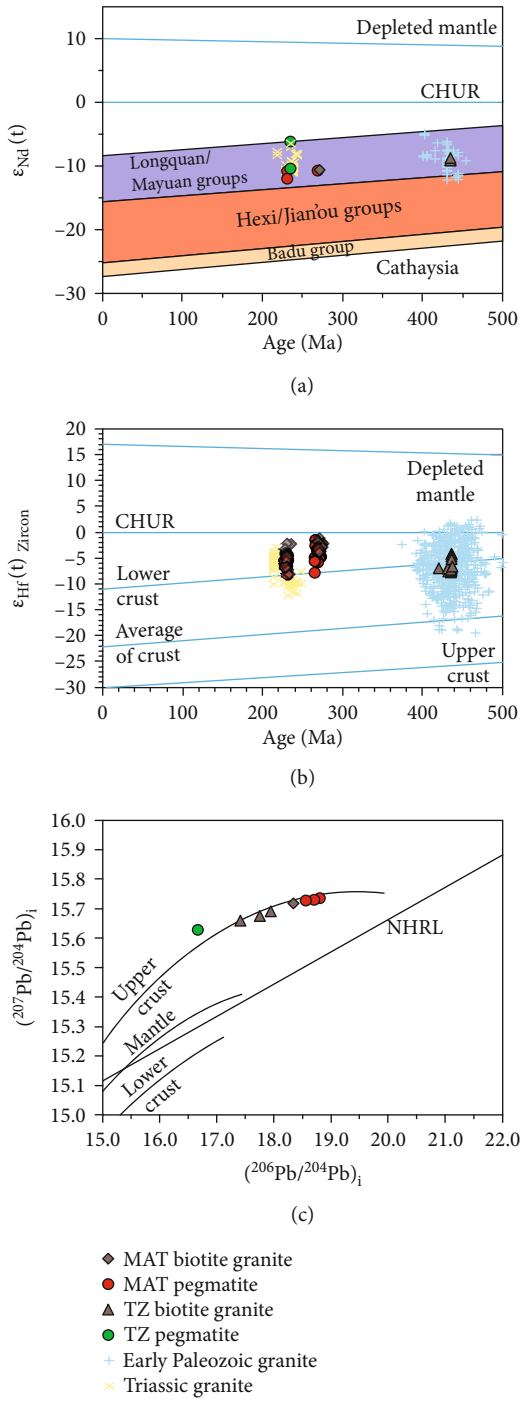

Figure 8: (a) Nd isotopic evolution of the Cathaysia Block (modified from [53]). (b) Hf isotopic evolution of magmatic zircons from the MAT and TZ biotite granites and pegmatites. Depleted mantle has present-day $^{176}Lu/^{177}Hf$ and $^{176}Hf/^{177}Hf$ ratios of 0.0384 and 0.28325, respectively [54]; chondrite (CHUR) has present-day $^{176}Lu/^{177}Hf$ and $^{176}Hf/^{177}Hf$ ratios of 0.0332 and 0.28277, respectively ([55] and references therein); continental upper crust has a present-day $^{176}Lu/^{177}Hf$ ratio of 0.0093; average crust has a present-day $^{176}Lu/^{177}Hf$ ratio of 0.015; and lower crust has a present-day $^{176}Lu/^{177}Hf$ ratio of 0.022 ([55] and references therein). (c) $(^{207}Pb/^{204}Pb)_i$ versus $(^{206}Pb/^{204}Pb)_i$ diagram for the MAT and TZ biotite granites and pegmatites. NHRL: Northern Hemisphere Reference Line [56]. Data sources for the early Paleozoic and Triassic granites are the same as for Figure 6.

model age of 1.9 Ga (Supplementary Table 2; Figure 8(a)). The ca. 230 Ma zircons of the MAT biotite granite wall rock (MAT-01) yield $\varepsilon_{Hf}(t)$ values of −8.0 to −2.1 with two-stage Hf model ages ranging from 1.8 to 1.4 Ga, whereas the ca. 270 Ma zircons of MAT-01 show relatively higher $\varepsilon_{Hf}(t)$ values of −3.9 to −1.0 and two-stage Hf model ages ranging from 1.5 to 1.4 Ga (Supplementary Table 3; Figure 8(b)). The TZ biotite granite wall rock (TZ-03) has zircon $\varepsilon_{Hf}(t)$

values of −7.7 to −4.1, with two-stage Hf model ages ranging from 1.9 to 1.7 Ga (Supplementary Table 3; Figure 8(b)). The MAT biotite granite wall rock (MAT-01) has $(^{206}Pb/^{204}Pb)_i$ ratios of 18.338, $(^{207}Pb/^{204}Pb)_i$ ratios of 15.718, and $(^{208}Pb/^{204}Pb)_i$ ratios of 38.728 (Supplementary Table 4; Figure 8(c)). The TZ biotite granite wall rocks have $(^{206}Pb/^{204}Pb)_i$ ratios of 17.410–17.941, $(^{207}Pb/^{204}Pb)_i$ ratios of 15.659–15.691, and $(^{208}Pb/^{204}Pb)_i$ ratios of 37.450–38.487 (Supplementary Table 4; Figure 8(c)).

5. Discussion

5.1. Magma Source and Evolution

5.1.1. MAT and TZ Biotite Granites. The whole-rock trace element and Nd–Pb isotopic compositions and zircon Hf isotopic compositions of the MAT and TZ biotite granites suggest that their source was dominated by Paleoproterozoic metasedimentary rocks in the middle crust. The MAT and TZ biotite granites have REE and trace element patterns that are similar to those of metasedimentary rock-derived, early Paleozoic, and Triassic granites in the SCB (Figures 7(a) and 7(b)). In particular, the Th contents (27.4–81.5 ppm) and Th/La ratios (0.60–1.00) of the MAT and TZ biotite granites are similar to those of the early Paleozoic and Triassic granites (Th = 7.56 – 84.2 ppm; Th/La = 0.31 – 1.47; [16, 20, 48]). In addition, the MAT and TZ biotite granites also have enriched whole-rock Nd and zircon Hf isotopic compositions that are similar to those of early Paleozoic and Triassic S-type granites with Nd model ages of $T_{2DM} = 1.9$ Ga and Hf model ages of $T_{2DM} = 2.4 - 1.7$ Ga in the SCB (Figures 8(a) and 8(b)). Moreover, the whole-rock Pb isotopic compositions of the MAT and TZ biotite granites plot along the upper crustal evolution line (Figure 8(c)).

We conclude from the above observations that the MAT and TZ biotite granites were mainly derived by partial melting of metasedimentary rocks in the middle crust. In general, metasedimentary rock-derived granitic magmas can be generated by either fluid-absent mica breakdown reactions or water-saturated melting of plagioclase [57]. In such a situation, a fluid-absent mica breakdown reaction would generate granitic melts with $K_2O > Na_2O$, whereas water-saturated melting of plagioclase would produce granitic melts with $K_2O < Na_2O$ ([58] and references therein). Therefore, the fact that the K_2O contents (4.5–7.0 wt.%) of the MAT and TZ biotite granites are higher than their Na_2O contents (0.6–3.0 wt.%; Supplementary Table 2) indicates that they were formed by melting as a result of fluid-absent mica breakdown in the middle crust.

The MAT biotite granite sample (MAT-01) and one TZ biotite granite sample (TZ-03) have SiO_2 contents (62.8–65.9 wt.%; Figure 6(a)) that are lower than those of experimental pure crustal melts ($SiO_2 \geq 70$ wt.%; [59]) produced by incongruent dehydration melting. This indicates, therefore, that metaigneous rocks or mantle-derived mafic magmas with $SiO_2 < 70$ wt.% were also present in the metasedimentary source area of the MAT and TZ biotite granites. The MAT and TZ biotite granites have relatively low Mg# values (27.4–34.5; Mg# = molar MgO/[molar MgO + molar FeO^T] × 100; assuming $FeO^T = 0.8998 \times Fe_2O_3{}^T$) and do not contain mafic microgranular enclaves (Figures 3(a) and 3(e); Supplementary Figures 1a–1b). We suggest, therefore, that other subordinate metaigneous rocks were also present in the metasedimentary source area of the MAT and TZ biotite granites.

5.1.2. MAT and TZ Pegmatites. The whole-rock Nd–Pb isotopic, zircon Hf isotopic, and mineral compositions of the MAT and TZ pegmatites indicate that their primary magmas were derived mainly by partial melting of Paleoproterozoic–Mesoproterozoic metasedimentary rocks in the middle crust. On an $\varepsilon_{Nd}(t)$ versus age diagram, the MAT and TZ pegmatites plot within the field of the Longquan–Mayuan groups (i.e., part of the basement of the Cathaysia Block) that have Nd model ages of $T_{2DM} = 2.0 - 1.5$ Ga (Figure 8(a); Supplementary Table 2). In addition, on an $\varepsilon_{Hf}(t)$ versus age diagram, the MAT pegmatites all plot below the chondritic evolution line, with Hf model ages of $T_{2DM} = 2.4 - 1.8$ Ga (Figure 8(b); Supplementary Table 3). The whole-rock Pb isotopic compositions of the MAT and TZ pegmatites are distributed along the upper crustal evolution line (Figure 8(c)). Furthermore, the MAT and TZ pegmatites contain euhedral tourmaline, muscovite, and garnet (Figures 3(c), 3(d), 3(g), and 3(h)), which generally crystallize from Al-saturated granitic magmas [60].

The whole-rock trace element characteristics of the MAT and TZ pegmatites suggest they experienced high degrees of fractional crystallization. The MAT and TZ pegmatites have relatively high contents of Nb (1.69–1649 ppm), Ta (0.23–183 ppm), Rb (7.38–5699 ppm), and Li (4.55–485 ppm; Supplementary Table 2), which were gradually enriched during fractional crystallization. Rubidium is a strongly incompatible element, whereas Sr and Ba are compatible in plagioclase and K-feldspar, respectively. Therefore, with fractional crystallization of a granitic magma, Rb is gradually concentrated in the residual magmas, whereas Sr and Ba are reduced in the residual magmas because of the removal of plagioclase and K-feldspar ([61] and references therein). Consequently, the Rb contents, Rb/Sr ratios, and K/Rb ratios can be used to evaluate the degree of fractional crystallization. In addition, in granitic melts, Ta^{5+} with an ionic radius of 0.73 Å forms a stronger covalent bond with oxygen than Nb^{5+} with its smaller ionic radius of 0.70 Å, which results in the relatively higher Ta concentration compared with Nb [62]. Therefore, the Nb/Ta ratios of granites gradually decrease with the degree of fractional crystallization [63, 64]. Given that Nb is more compatible in biotite than Ta, fractional crystallization of biotite could also decrease the Nb/Ta ratios in the residual melts [65]. Moreover, during fractional crystallization, Zr^{4+} with an ionic radius of 0.80 Å in zircon is gradually replaced by Th^{4+}, which has a similar ionic radius of 0.95 Å [66]. Therefore, the Nb/Ta and Zr/Hf ratios would decrease during fractional crystallization [25]. On the Rb–Ba–Sr triangular diagram, the MAT and TZ pegmatites all plot in the highly fractionated granite field (Figure 9(a)). In addition, the plots of the MAT and TZ pegmatites on the K/Rb versus SiO_2, Nb/Ta versus Rb/Sr, and Zr/Hf versus Rb/

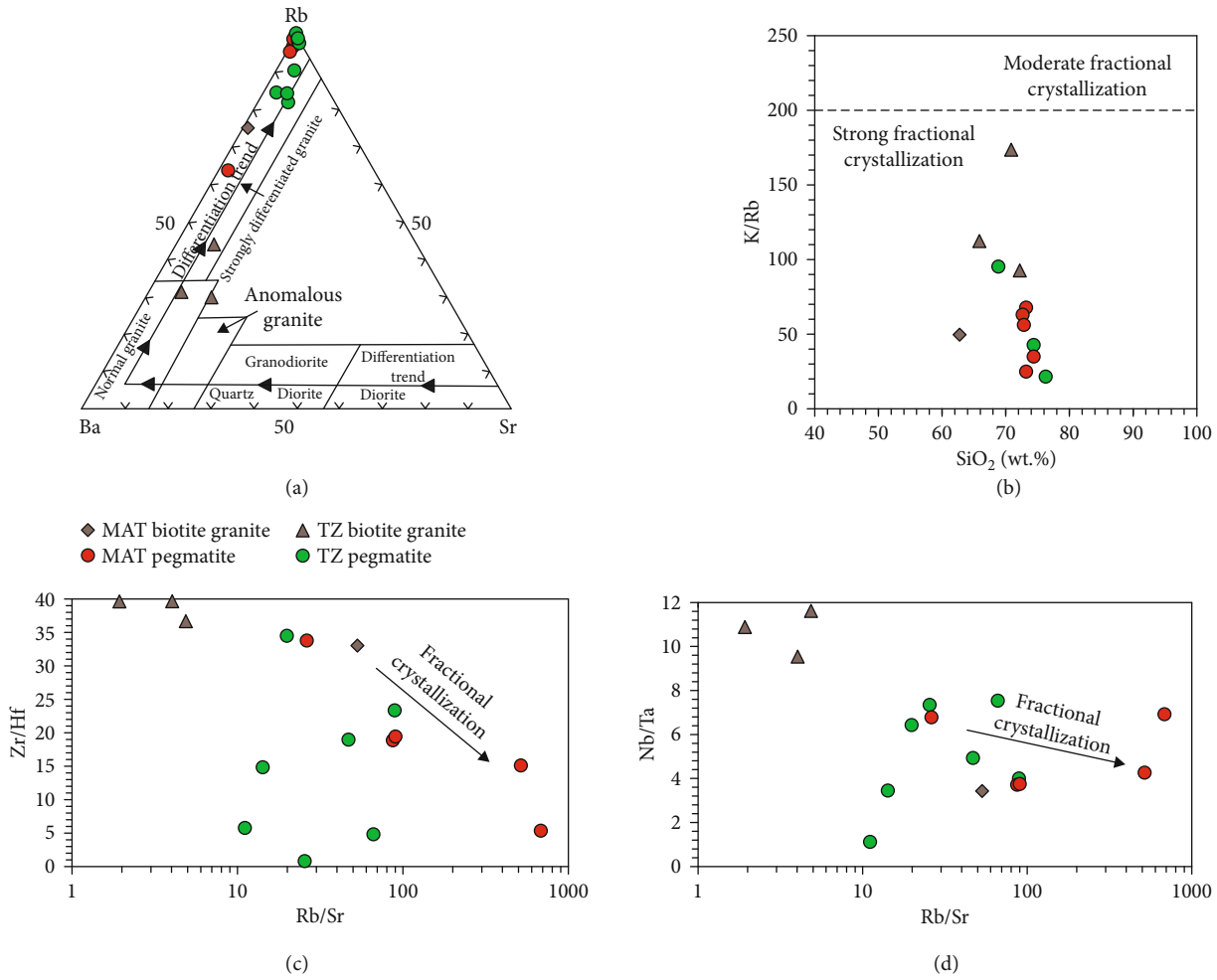

Figure 9: Plots of (a) Rb–Ba–Sr (modified from [67]), (b) K/Rb versus SiO_2 (modified from [68]), (c) Zr/Hf versus Rb/Sr, and (d) Nb/Ta versus Rb/Sr for the MAT and TZ biotite granites and pegmatites. We do not plot five pegmatite samples (TZ-04, TZ-05, TZ-07, TZ-08, and TZ-09) in (b), because they are cumulates of K-feldspar, albite, muscovite, and quartz.

Sr diagrams indicate that these rocks represent high degrees of fractional crystallization (Figures 9(b)–9(d)).

The MAT pegmatites are hosted by the MAT biotite granite (Figure 3(a); Supplementary Figures 1a–1b), which indicates these rocks have a cogenetic relationship [3]. In addition, the MAT pegmatites and biotite granite have broadly parallel REE and trace element patterns (Figures 7(a) and 7(b)). Therefore, the MAT pegmatites are possibly the fractional crystallization products of the MAT biotite granite [69]. The results of trace element fractional-crystallization modeling, using the MAT biotite granite (MAT-01) as the initial magma, suggest that MAT pegmatite MAT-04 could have been formed by the removal of small amounts of biotite (<10%; Figures 10(a) and 10(b)). Likewise, using MAT biotite granite MAT-01 as the initial magma, four other MAT pegmatites (MAT-02, 03, 05, and 06) could have been formed by the removal of 30–50% K-feldspar (Figures 10(a) and 10(b)). In addition to major rock-forming minerals, the MAT pegmatites could have been formed by fractionation of apatite, titanite, monazite, and allanite, as revealed by plots of whole-rock $(La/Yb)_{CN}$ versus La and zircon La/Yb versus La (Figures 10(c) and 10(d)), assuming the MAT biotite granite was the parental magma. Moreover, the plots of zircon Ta versus Nb for the MAT pegmatites also suggest that fractional crystallization of columbite-group minerals occurred (Figure 10(e)).

The TZ pegmatites are significantly younger (235 Ma) than the TZ biotite granites (435 Ma; Figures 5(d) and 5(e)). Therefore, the TZ pegmatites may not have a genetic relationship with their biotite granite wall rocks, and the parental granites that are related to the TZ pegmatites may not be exposed at the surface. Nonetheless, the zircon Ta versus Nb diagram for the TZ pegmatites suggests they underwent fractional crystallization of columbite-group minerals (Figure 10(f)). Because the MAT and TZ pegmatites represent high degrees of fractional crystallization, we suggest that these pegmatites have the potential for rare metal (Nb, Ta, Be, and Li) mineralization. During fractional crystallization, the Nb, Ta, Be, and Rb contents of the MAT and TZ granitic magmas would have increased, along with a gradual increase in Li and F contents [63]. Therefore, we

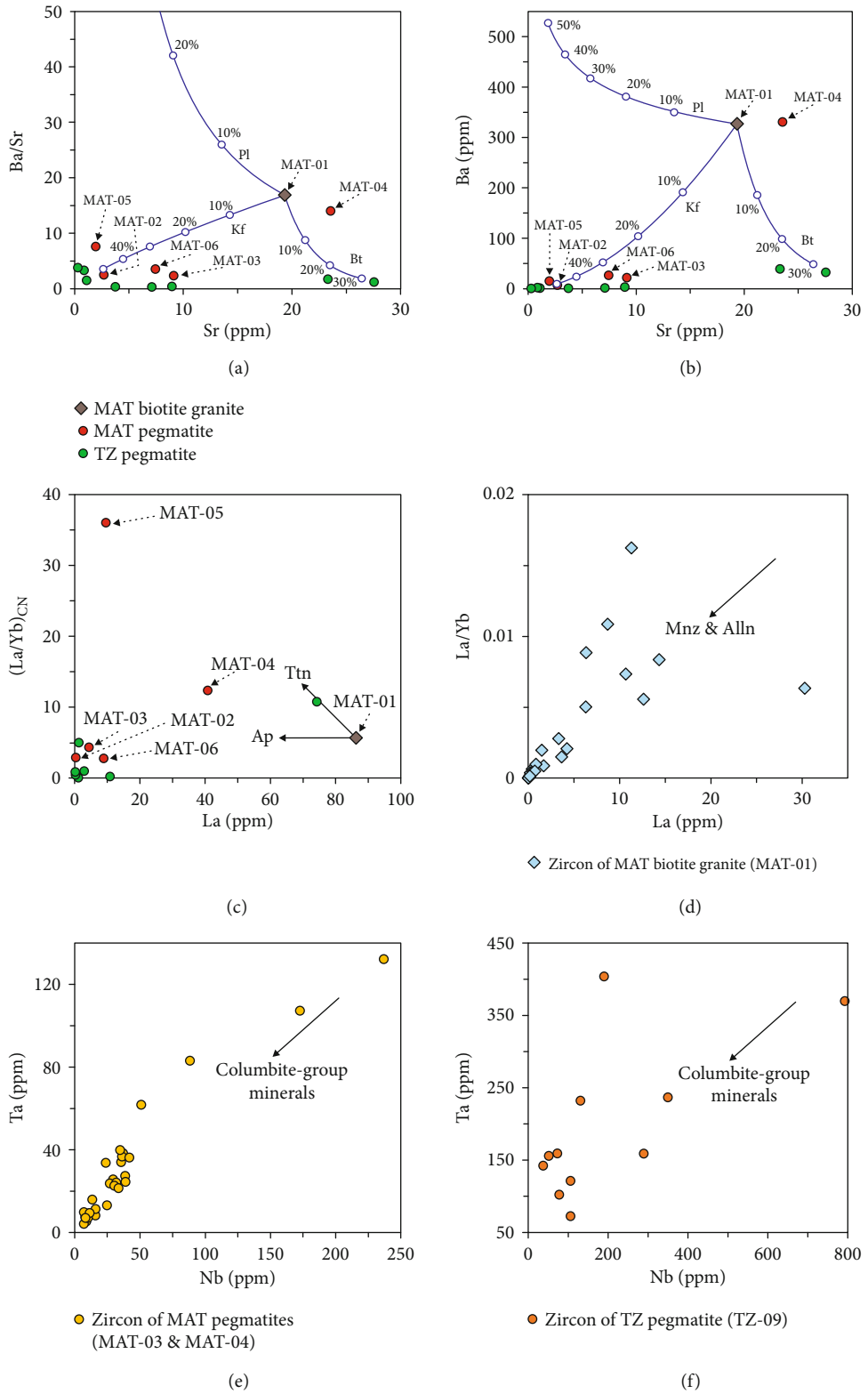

Figure 10: Plots of whole-rock (a) Ba/Sr versus Sr, (b) Ba versus Sr, and (c) $(La/Yb)_{CN}$ versus La (modified from [70]) for the MAT biotite granite and pegmatites and the TZ pegmatites. Partition coefficients and the calculated Sr and Ba contents in (a) and (b) are given in Supplementary Table 5. Plots of zircon (d) La/Yb versus La and (e, f) Ta versus Nb (modified from [71]) for the MAT biotite granite and pegmatites and the TZ pegmatites. Zircon trace element data are listed in Supplementary Table 6. Mineral abbreviations: Pl: plagioclase; Kf: K-feldspar; Bt: biotite; Ttn: titanite; Ap: apatite; Mnz: monazite; Alln: allanite.

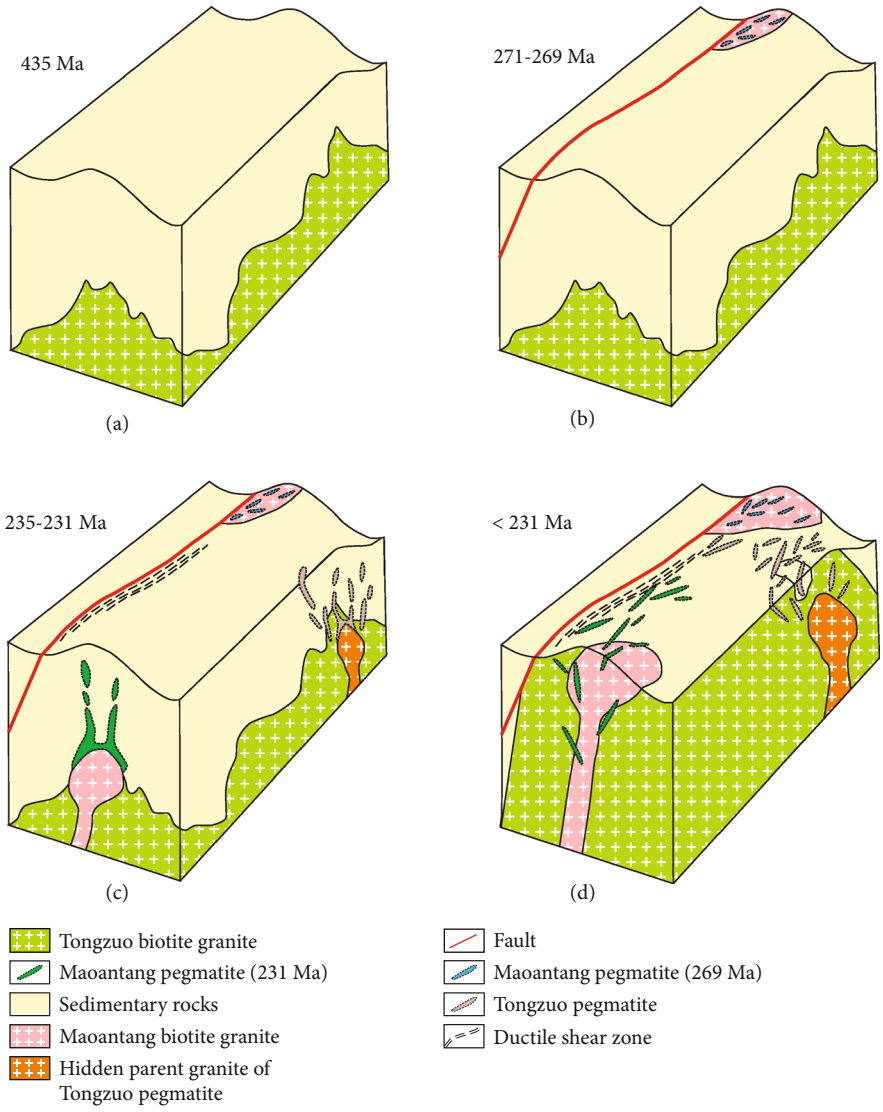

FIGURE 11: Petrogenetic model for the MAT and TZ biotite granites and pegmatites. (a) Formation of early Paleozoic TZ biotite granites in response to double-thickening or orogenic collapse of an intracontinental orogen. (b) Formation of the late Paleozoic MAT biotite granite and pegmatites during the post-orogenic stage. (c) Formation of the Triassic MAT and TZ pegmatites during the intracontinental orogeny. Granites cogenetic with the TZ pegmatites may be hidden deeper in the crust. (d) Denudation of the MAT and TZ biotite granites and pegmatites after 231 Ma. The pictures are not to scale.

conclude that the MAT and TZ areas in the middle of the Yuechengling pluton are promising targets for rare metal exploration.

5.2. Heat Source. Based on a recent review of regional geological data ([72] and references therein), it has been suggested that the early Paleozoic intracontinental orogeny of the SCB can be divided into three stages involving double thickening of the crust (460–435 Ma), orogenic collapse (441–415 Ma), and postorogenic (<415 Ma). Therefore, the early Paleozoic TZ biotite granites probably formed during the double-thickening or orogenic collapse stages. After the Middle or Late Devonian, the entire South China region evolved into a stable littoral–neritic depositional environment, characterized by a carbonate depositional platform with limestones, dolomites, black cherts, and minor sandstones and mudstones ([15] and references therein). Therefore, the late Paleozoic MAT biotite granite possibly formed in a postorogenic setting. The SCB was in a compressional tectonic setting during the Middle–Late Triassic [18–20, 22, 23]. As a consequence, the Late Triassic MAT and TZ pegmatites probably formed during the double thickening of the crust. Heat is generated via the decay of radioactive elements in the sedimentary rocks (e.g., [20, 73]), possibly enhanced by heating from mantle-derived mafic magmas in adjacent regions [74], induced dehydration partial melting of the metasedimentary, and associated subordinate metaigneous rocks. This generated the primary magmas of the MAT and TZ biotite granites, as well as the hidden parental granites of the TZ pegmatites (Figures 11(a)–11(c)). The MAT pegmatites were fractional crystallization products of the MAT biotite granite (Figures 11(b)–11(d)). The TZ

pegmatites were formed by fractional crystallization of hidden parental granites (Figures 11(c) and 11(d)).

6. Conclusions

(1) LA–ICP–MS zircon U–Pb dating demonstrates that the MAT pegmatites formed during the Permian (269 Ma) and Triassic (231 Ma). The MAT biotite granite wall rock records two stages of magmatic activity (271 and 231 Ma) that were coeval with the Permian and Triassic pegmatites. The TZ pegmatites probably formed during the Triassic (235 Ma), whereas the TZ biotite granite wall rock formed during the Silurian (435 Ma)

(2) The MAT and TZ biotite granites were derived mainly from Paleoproterozoic metasedimentary rocks in the middle crust. The MAT pegmatites are the fractional crystallization products of the MAT biotite granite, whereas the TZ pegmatites were formed by fractional crystallization of hidden parental S-type granites

(3) Because the MAT and TZ pegmatites record high degrees of fractional crystallization, they have the potential for rare metal (Nb, Ta, Be, and Li) mineralization

Data Availability

Data are uploaded as supplementary files and can be found when required. All the data are obtained at the Guangxi Key Laboratory of Hidden Metallic Ore Deposits Exploration, Guilin University of Technology, China.

Disclosure

This is a contribution to the Guangxi Key Mineral Resources Deep Exploration Talent Highland.

Conflicts of Interest

The authors declare that they have no known competing financial interests or personal relationships that could have appeared to influence the work reported in this paper.

Acknowledgments

Jin-Heng Liu of the Guangzhou Institute of Geochemistry, Chinese Academy of Sciences, is thanked for helpful suggestions and discussions. Financial support for this research was provided by the Natural Science Fund for Distinguished Young Scholars of Guangxi Province (Grants 2018GXNSFFA281009 and 2019GXNSFFA245005), National Natural Science Foundation of China (Grants 92055208, 41862003, and 42173067), Natural Science Foundation of Guangxi Province for Young Scholars (Grants 2022GXNSFBA035538 and 2022GXNSFBA035463), Guangxi Science Innovation Base Construction Foundation (Grant ZY21195031), Fifth Bagui Scholar Innovation Project of Guangxi Province (to Ji-Feng Xu), and Scientific Research Foundation of Guilin University of Technology (Grant RD2100001797).

Supplementary Materials

Supplementary 1. Supplementary Figure 1: (a–b) field photographs of the MAT biotite granites and pegmatites. (c–d) Field photographs of the TZ pegmatites. (e–f) Crosspolarized light photomicrographs of the TZ biotite granites. Qz: quartz; Bt: biotite; Pl: plagioclase; Mus: muscovite.

Supplementary 2. Supplementary Table 1: zircon U–Pb isotope data for granites–pegmatites in the Mao'antang–Tongzuo area.

Supplementary 3. Supplementary Table 2: whole-rock major (wt.%) and trace (ppm) element and Sr–Nd isotope data for granites–pegmatites in the Mao'antang–Tongzuo area.

Supplementary 4. Supplementary Table 3: zircon Hf isotope data for granites–pegmatites in the Mao'antang–Tongzuo area.

Supplementary 5. Supplementary Table 4: whole-rock Pb isotope data for granites–pegmatites in the Mao'antang–Tongzuo area.

Supplementary 6. Supplementary Table 5: initial composition, partition coefficients, and other input parameters for fractional crystallization modeling of Sr and Ba contents in the Mao'antang granites–pegmatites.

Supplementary 7. Supplementary Table 6: zircon trace element data for granites–pegmatites in the Mao'antang–Tongzuo area.

References

[1] P. Černý, D. London, and M. Novák, "Granitic pegmatites as reflections of their sources," *Elements*, vol. 8, no. 4, pp. 289–294, 2012.

[2] R. L. Linnen, M. Van Lichtervelde, and P. Černý, "Granitic pegmatites as sources of strategic metals," *Elements*, vol. 8, no. 4, pp. 275–280, 2012.

[3] D. London, "Ore-forming processes within granitic pegmatites," *Ore Geology Reviews*, vol. 101, pp. 349–383, 2018.

[4] B. Chen, C. Huang, and H. Zhao, "Lithium and Nd isotopic constraints on the origin of Li-poor pegmatite with implications for Li mineralization," *Chemical Geology*, vol. 551, article 119769, 2020.

[5] W. C. Fuchsloch, P. A. Nex, and J. A. Kinnaird, "Classification, mineralogical and geochemical variations in pegmatites of the Cape Cross-Uis pegmatite belt, Namibia," *Lithos*, vol. 296-299, pp. 79–95, 2018.

[6] B. Zheng, B. Chen, K. Sun, and C. Huang, "Tourmaline as a recorder of the magmatic-hydrothermal evolution in the formation of pegmatite: in-situ elemental and boron isotopic compositions of tourmaline from the Qinghe pegmatite," *Journal of Asian Earth Sciences*, vol. 231, Article ID 105224, 2022.

[7] Z. H. Lv, H. Zhang, and Y. Tang, "Anatexis origin of rare metal/earth pegmatites: evidences from the Permian pegmatites in the Chinese Altai," *Lithos*, vol. 380-381, article 105865, 2021.

[8] J. W. Mao, Y. B. Cheng, M. H. Chen, and F. Pirajno, "Major types and time–space distribution of Mesozoic ore deposits in South China and their geodynamic settings," *Mineralium Deposita*, vol. 48, no. 3, pp. 267–294, 2013.

[9] H. Chen, M. Feng, Z. Q. Kang, W. Fu, and Z. H. Feng, "Characteristics of garnets in pegmatites of Mao'antang, Northeast Guangxi, and their implications for magmatic evolution," *Earth Science*, vol. 45, pp. 2059–2076, 2020.

[10] Y. J. Wang, W. M. Fan, G. W. Zhang, and Y. H. Zhang, "Phanerozoic tectonics of the South China Block: key observations and controversies," *Gondwana Research*, vol. 23, no. 4, pp. 1273–1305, 2013.

[11] X. H. Li, Y. X. Wang, Z. H. Zhao, D. F. Chen, and H. Zhang, "SHRIMP U-Pb zircon geochronology for amphibolite from the Precambrian basement in SW Zhejiang and NW Fujian Province," *Geochimica*, vol. 27, pp. 327–334, 1998.

[12] J. H. Yu, S. Y. O'Reilly, M. F. Zhou, W. L. Griffin, and L. J. Wang, "U–Pb geochronology and Hf–Nd isotopic geochemistry of the Badu Complex, Southeastern China: implications for the Precambrian crustal evolution and paleogeography of the Cathaysia Block," *Precambrian Research*, vol. 222-223, pp. 424–449, 2012.

[13] Z. X. Yuan, L. S. Wu, Z. Q. Zhang, and X. J. Ye, "The Sm-Nd, Rb-Sr isotopic age-dating of Mayuan group in northern Fujian," *Acta Petrologica et Mineralogica*, vol. 10, pp. 127–132, 1991.

[14] G. Y. Wu, J. D. Li, Q. J. Che, Q. H. Xiao, X. S. Tang, and H. G. Peng, "Sm-Nd dating and genesis of the Jianxichong Group metamorphic volcanic rocks in Northeast Hunan Group," *Geoscience*, vol. 18, pp. 339–345, 2004.

[15] L. S. Shu, B. Wang, P. A. Cawood, M. Santosh, and Z. Q. Xu, "Early Paleozoic and Early Mesozoic intraplate tectonic and magmatic events in the Cathaysia Block, South China," *Tectonics*, vol. 34, no. 8, pp. 1600–1621, 2015.

[16] Y. J. Wang, A. M. Zhang, W. M. Fan et al., "Kwangsian crustal anatexis within the eastern South China Block: geochemical, zircon U–Pb geochronological and Hf isotopic fingerprints from the gneissoid granites of Wugong and Wuyi–Yunkai Domains," *Lithos*, vol. 127, no. 1-2, pp. 239–260, 2011.

[17] L. G. Wu, X. H. Li, W. H. Yao, X. X. Ling, and K. Lu, "Insights into polyphase Phanerozoic tectonic events in SE China: integrated isotopic microanalysis of detrital zircon and monazite," *Lithosphere*, vol. 2020, 17 pages, 2020.

[18] L. Qing, Y. H. Jiang, and F. G. Du, "Petrogenesis and tectonic significance of early Indosinian A-type granites in the Xinxing pluton, southern South China," *Mineralogy and Petrology*, vol. 114, no. 3, pp. 217–242, 2020.

[19] Y. J. Wang, W. M. Fan, P. A. Cawood, S. C. Ji, T. P. Peng, and X. Y. Chen, "Indosinian high-strain deformation for the Yunkaidashan tectonic belt, South China: kinematics and $^{40}Ar/^{39}Ar$ geochronological constraints," *Tectonics*, vol. 26, no. 6, pp. 1–21, 2007.

[20] Y. J. Wang, W. M. Fan, M. Sun, X. Q. Liang, Y. H. Zhang, and T. P. Peng, "Geochronological, geochemical and geothermal constraints on petrogenesis of the Indosinian peraluminous granites in the South China Block: a case study in the Hunan Province," *Lithos*, vol. 96, no. 3-4, pp. 475–502, 2007.

[21] X. M. Zhou, T. Sun, W. Z. Shen, L. S. Shu, and Y. L. Niu, "Petrogenesis of Mesozoic granitoids and volcanic rocks in South China: a response to tectonic evolution," *Episodes*, vol. 29, no. 1, pp. 26–33, 2006.

[22] Z. X. Li and X. H. Li, "Formation of the 1300-km-wide intracontinental orogen and postorogenic magmatic province in Mesozoic South China: a flat-slab subduction model," *Geology*, vol. 35, no. 2, pp. 179–182, 2007.

[23] J. R. Mao, H. M. Ye, K. Liu et al., "The Indosinian collision-extension event between the South China Block and the Palaeo-Pacific plate: evidence from Indosinian alkaline granitic rocks in Dashuang, eastern Zhejiang, South China," *Lithos*, vol. 172-173, pp. 81–97, 2013.

[24] X. H. Li, Z. X. Li, W. X. Li et al., "U–Pb zircon, geochemical and Sr–Nd–Hf isotopic constraints on age and origin of Jurassic I- and A-type granites from central Guangdong, SE China: a major igneous event in response to foundering of a subducted flat-slab?," *Lithos*, vol. 96, no. 1-2, pp. 186–204, 2007.

[25] J. Li, X. L. Huang, G. J. Wei et al., "Lithium isotope fractionation during magmatic differentiation and hydrothermal processes in rare-metal granites," *Geochimica et Cosmochimica Acta*, vol. 240, pp. 64–79, 2018.

[26] X. Liu, Q. Wang, L. Ma et al., "Petrogenesis of Late Jurassic two-mica granites and associated diorites and syenite porphyries in Guangzhou, SE China," *Lithos*, vol. 364-365, article 105537, 2020.

[27] W. D. Chen, W. L. Zhang, R. C. Wang et al., "A study on the Dushiling tungsten-copper deposit in the Miao'ershan-Yuechengling area, Northern Guangxi, China: implications for variations in the mineralization of multi-aged composite granite plutons," *Science China Earth Sciences*, vol. 59, no. 11, pp. 2121–2141, 2016.

[28] Y. Chu, W. Lin, M. Faure, Q. C. Wang, and W. B. Ji, "Phanerozoic tectonothermal events of the Xuefengshan Belt, central South China: Implications from UPb age and LuHf determinations of granites," *Lithos*, vol. 150, pp. 243–255, 2012.

[29] E. N. Tian, R. C. Wang, L. Xie, W. L. Zhang, X. D. Che, and R. Q. Zhang, "Mineralogy and geochemistry of the newly discovered Late Mesozoic granite- pegmatite and associated Sn-Nb-Ta-Be mineralization in the Miao'ershan- Yuechengling composite batholith, northern Guangxi, South China," *Journal of Asian Earth Sciences*, vol. 190, article 104149, 2020.

[30] K. D. Zhao, S. Y. Jiang, T. Sun, W. F. Chen, H. F. Ling, and P. R. Chen, "Zircon U-Pb dating, trace element and Sr-Nd-Hf isotope geochemistry of Paleozoic granites in the Miao'ershan-Yuechengling batholith, South China: implication for petrogenesis and tectonic-magmatic evolution," *Journal of Asian Earth Sciences*, vol. 74, pp. 244–264, 2013.

[31] S. B. Chen, J. M. Fu, S. Cui, Y. Y. Lu, L. Y. Ma, and A. S. Liu, "Zircon U-Pb chronology, geochemistry of the Indonesian granitic rocks from northern Yuechengling batholith in Guangxi-Hunan junction," *Earth Science*, vol. 43, pp. 2330–2349, 2018.

[32] K. D. Zhao, S. Y. Jiang, H. F. Ling et al., "Late Triassic U-bearing and barren granites in the Miao'ershan batholith, South China: petrogenetic discrimination and exploration significance," *Ore Geology Reviews*, vol. 77, pp. 260–278, 2016.

[33] N. J. Pearce, W. T. Perkins, J. A. Westgate et al., "A compilation of new and published major and trace element data for NIST SRM 610 and NIST SRM 612 glass reference materials," *Geostandards and Geoanalytical Research*, vol. 21, no. 1, pp. 115–144, 1997.

[34] J. Sláma, J. Koler, D. J. Condon et al., "Plešovice zircon — a new natural reference material for U–Pb and Hf isotopic microanalysis," *Chemical Geology*, vol. 249, no. 1-2, pp. 1–35, 2008.

[35] Y. S. Liu, Z. C. Hu, S. Gao et al., "*In situ* analysis of major and trace elements of anhydrous minerals by LA- ICP-MS without applying an internal standard," *Chemical Geology*, vol. 257, no. 1-2, pp. 34–43, 2008.

[36] K. R. Ludwig, *Isoplot 3.75: a geochronological toolkit for Microsoft Excel*, vol. 5, Berkeley geochronology center special Publication, 2012.

[37] X. J. Liu, J. F. Xu, P. R. Castillo et al., "The Dupal isotopic anomaly in the southern Paleo-Asian Ocean: Nd-Pb isotope evidence from ophiolites in Northwest China," *Lithos*, vol. 189, pp. 185–200, 2014.

[38] Z. G. Zhang, X. J. Liu, W. J. Xiao et al., "Geochemistry and Sr-Nd-Hf-Pb isotope systematics of late Carboniferous sanukitoids in northern West Junggar, NW China: implications for initiation of ridge-subduction," *Gondwana Research*, vol. 99, pp. 204–218, 2021.

[39] W. Zhang and Z. C. Hu, "Estimation of isotopic reference values for pure materials and geological reference materials," *Atomic Spectroscopy*, vol. 41, no. 3, pp. 93–102, 2020.

[40] W. Todt, R. A. Cliff, A. Hanser, and A. W. Hofmann, "Evaluation of a ^{202}Pb–^{205}Pb double spike for high-precision lead isotope analysis," *Geophysical Monograph Series*, vol. 95, pp. 429–437, 2013.

[41] F. Y. Wu, Y. H. Yang, L. W. Xie, J. H. Yang, and P. Xu, "Hf isotopic compositions of the standard zircons and baddeleyites used in U-Pb geochronology," *Chemical Geology*, vol. 234, no. 1-2, pp. 105–126, 2006.

[42] M. L. A. Morel, O. Nebel, Y. J. Nebel-Jacobsen, J. S. Miller, and P. Z. Vroon, "Hafnium isotope characterization of the GJ-1 zircon reference material by solution and laser-ablation MC-ICPMS," *Chemical Geology*, vol. 255, no. 1-2, pp. 231–235, 2008.

[43] P. Hoskin and L. Black, "Metamorphic zircon formation by solid-state recrystallization of protolith igneous zircon," *Journal of Metamorphic Geology*, vol. 18, no. 4, pp. 423–439, 2000.

[44] R. W. Le Maitre, *Igneous Rocks: A. Classification and Glossary of Terms*, Cambridge Univ, Cambridge, 2002.

[45] A. Peccerillo and S. R. Taylor, "Geochemistry of Eocene calc-alkaline volcanic rocks from the Kastamonu area, Northern Turkey," *Contributions to Mineralogy and Petrology*, vol. 58, no. 1, pp. 63–81, 1976.

[46] P. D. Maniar and P. M. Piccoli, "Tectonic discrimination of granitoids," *Geological Society of America Bulletin*, vol. 101, no. 5, pp. 635–643, 1989.

[47] C. D. Frost, J. M. Bell, B. R. Frost, and K. R. Chamberlain, "Crustal growth by magmatic underplating: isotopic evidence from the northern Sherman batholith," *Geology*, vol. 29, no. 6, pp. 515–518, 2001.

[48] F. F. Zhang, Y. J. Wang, A. M. Zhang, W. M. Fan, Y. Z. Zhang, and J. W. Zi, "Geochronological and geochemical constraints on the petrogenesis of Middle Paleozoic (Kwangsian) massive granites in the eastern South China Block," *Lithos*, vol. 150, pp. 188–208, 2012.

[49] P. Gao, Z. F. Zhao, and Y. F. Zheng, "Petrogenesis of Triassic granites from the Nanling Range in South China: implications for geochemical diversity in granites," *Lithos*, vol. 210-211, pp. 40–56, 2014.

[50] S.-S. Sun and W. F. McDonough, "Chemical and isotopic systematics of oceanic basalts: implications for mantle composition and processes," *Geological Society, London, Special Publications*, vol. 42, no. 1, pp. 313–345, 1989.

[51] X. Liu, H. Liang, Q. Wang et al., "Early Cretaceous Sn-bearing granite porphyries, A-type granites, and rhyolites in the Mikengshan-Qingxixiang-Yanbei area, South China: Petrogenesis and implications for ore mineralization," *Journal of Asian Earth Sciences*, vol. 235, article 105274, 2022.

[52] Z. W. Bao and Z. H. Zhao, "Geochemistry of mineralization with exchangeable REY in the weathering crusts of granitic rocks in South China," *Ore Geology Reviews*, vol. 33, no. 3-4, pp. 519–535, 2008.

[53] J. F. Chen and B. M. Jahn, "Crustal evolution of southeastern China: Nd and Sr isotopic evidence," *Tectonophysics*, vol. 284, no. 1-2, pp. 101–133, 1998.

[54] W. L. Griffin, N. J. Pearson, E. Belousova et al., "The Hf isotope composition of cratonic mantle: LAM-MC-ICPMS analysis of zircon megacrysts in kimberlites," *Geochimica et Cosmochimica Acta*, vol. 64, no. 1, pp. 133–147, 2000.

[55] F. Y. Wu, X. H. Li, Y. F. Zheng, and S. Gao, "Lu-Hf isotopic systematics and their applications in petrology," *Acta Petrologica Sinica*, vol. 23, pp. 185–220, 2007.

[56] S. R. Hart, "A large-scale isotope anomaly in the Southern Hemisphere mantle," *Nature*, vol. 309, no. 5971, pp. 753–757, 1984.

[57] Y. H. Jiang and S. Q. Zhu, "Petrogenesis of the Late Jurassic peraluminous biotite granites and muscovite-bearing granites in SE China: geochronological, elemental and Sr–Nd–O–Hf isotopic constraints," *Contributions to Mineralogy and Petrology*, vol. 172, no. 11-12, pp. 1–27, 2017.

[58] H. Q. Huang, X. H. Li, Z. X. Li, and W. X. Li, "Formation of the Jurassic South China Large Granitic Province: insights from the genesis of the Jiufeng pluton," *Chemical Geology*, vol. 401, pp. 43–58, 2015.

[59] A. E. Patiño Douce, "What do experiments tell us about the relative contributions of crust and mantle to the origin of granitic magmas?," *Geological Society, London, Special Publications*, vol. 168, no. 1, pp. 55–75, 1999.

[60] B. Barbarin, "A review of the relationships between granitoid types, their origins and their geodynamic environments," *Lithos*, vol. 46, no. 3, pp. 605–626, 1999.

[61] Z. Y. Zhang, J. L. Ma, L. Zhang, Y. Liu, and G. J. Wei, "Rubidium purificationviaa single chemical column and its isotope measurement on geological standard materials by MC-ICP-MS," *Journal of Analytical Atomic Spectrometry*, vol. 33, no. 2, pp. 322–328, 2018.

[62] W. S. Horng and P. C. Hess, "Partition coefficients of Nb and Ta between rutile and anhydrous haplogranite melts," *Contributions to Mineralogy and Petrology*, vol. 138, no. 2, pp. 176–185, 2000.

[63] J. Li and X. L. Huang, "Mechanism of Ta-Nb enrichment and magmatic evolution in the Yashan granites, Jiangxi Province, South China," *Acta Petrologica Sinica*, vol. 29, pp. 4311–4322, 2013.

[64] L. Xie, R. C. Wang, X. D. Che, F. F. Huang, S. Erdmann, and W. L. Zhang, "Tracking magmatic and hydrothermal Nb-Ta-W-Sn fractionation using mineral textures and composition: a case study from the late Cretaceous Jiepailing ore district in the Nanling Range in South China," *Ore Geology Reviews*, vol. 78, pp. 300–321, 2016.

[65] C. Ballouard, M. Poujol, P. Boulvais, Y. Branquet, R. Tartese, and J. L. Vigneresse, "Nb-Ta fractionation in peraluminous granites: a marker of the magmatic-hydrothermal transition," *Geology*, vol. 44, no. 3, pp. 231–234, 2016.

[66] R. C. Wang, F. Fontan, X. M. Chen et al., "Accessory minerals in the Xihuashan Y-enriched granitic complex, southern China: a record of magmatic and hydrothermal stages of evolution," *The Canadian Mineralogist*, vol. 41, no. 3, pp. 727–748, 2003.

[67] E. L. Bouseily and A. A. El Sokkary, "The relation between Rb, Ba and Sr in granitic rocks," *Chemical Geology*, vol. 16, no. 3, pp. 207–219, 1975.

[68] P. Blevin, "Redox and compositional parameters for interpreting the granitoid metallogeny of eastern Australia: implications for gold-rich ore systems," *Resource Geology*, vol. 54, no. 3, pp. 241–252, 2004.

[69] L. Ma, A. C. Kerr, Q. Wang, Z. Q. Jiang, and W. L. Hu, "Early Cretaceous (~ 140 Ma) aluminous A-type granites in the Tethyan Himalaya, Tibet: products of crust-mantle interaction during lithospheric extension," *Lithos*, vol. 300-301, pp. 212–226, 2018.

[70] Z. Y. Yang, Q. Wang, C. F. Zhang et al., "Cretaceous (~100 Ma) high-silica granites in the Gajin area, Central Tibet: petrogenesis and implications for collision between the Lhasa and Qiangtang Terranes," *Lithos*, vol. 324-325, pp. 402–417, 2019.

[71] M. Xu, X. X. Duan, B. Chen, Z. Q. Wang, Y. J. Chen, and X. F. Li, "Trace elements in zircon: constrain on magmatic differentiation: a case study on Triassic Wangxianling granitoid in southern Hunan Province," *Geological Review*, vol. 66, pp. 665–685, 2020.

[72] X. Liu, Q. Wang, L. Ma, J. H. Yang, Y. M. Ma, and T. Y. Huang, "Early Paleozoic and Late Mesozoic crustal reworking of the South China Block: insights from Early Silurian biotite granodiorites and Late Jurassic biotite granites in the Guangzhou area of the south-east Wuyi-Yunkai orogeny," *Journal of Asian Earth Sciences*, vol. 219, article 104890, 2021.

[73] Z. X. Li, X. H. Li, J. A. Wartho et al., "Magmatic and metamorphic events during the early Paleozoic Wuyi-Yunkai orogeny, southeastern South China: new age constraints and pressure-temperature conditions," *GSA Bulletin*, vol. 122, no. 5-6, pp. 772–793, 2010.

[74] W. J. Xu and X. S. Xu, "Early Paleozoic intracontinental felsic magmatism in the South China Block: petrogenesis and geodynamics," *Lithos*, vol. 234-235, pp. 79–92, 2015.